Journal of Translational Medicine

RESEARCH

Open Access

A pathology-to-single-cell framework links SPP1$^+$ M2 macrophages with NETs-prone high-risk niches in HCC

Ruixiang Li[1†], Yuheng Gu[1†], Shi Huang[1†], Shiya Zeng[1†], Xuanchen Zhou[1], Weiqi Luo[1], Zhuo Wen[1], Wenjing Chen[1], Cheng Chen[1], Lantian Cui[1], Hongyu Duan[2] and Mengfan Zhao[3*]

Abstract

Background Neutrophil extracellular traps (NETs) facilitate hepatocellular carcinoma (HCC) progression, but the upstream cellular organizers and the histopathological correlates of NETosis-prone niches remain poorly defined. We aimed to build a pathology-to-single-cell framework to (i) quantify NETs-associated risk from routine whole-slide images (WSI) and (ii) nominate candidate organizer cells and mechanisms, focusing on SPP1$^+$ M2 macrophages.

Methods We integrated WSI, bulk transcriptomics, single-cell RNA-seq, spatial transcriptomics, and germline association data. NETs activity was quantified using gene-set scoring and aligned with WSI-derived morphology features (e.g. texture, stromal boundary disruption, and tumor–stroma interface complexity) to train and validate a prognostic model using regularized feature selection and survival machine learning. A 26,928-cell single-cell atlas was constructed to annotate macrophage states and neutrophil subsets, followed by trajectory inference to model macrophage polarization dynamics. Cell–cell communication was evaluated by ligand–receptor co-expression networks, and pathway/metabolic programs were inferred using multi-method enrichment and flux estimation. Spatial co-localization and neighborhood effects were assessed by deconvolution and spatial interaction modeling. Finally, network-based target prioritization was performed to highlight druggable nodes and candidate intervention pathways.

Results The WSI-derived NETs risk score stratified overall survival in training and validation cohorts (HR ≈ 8.48 and ≈6.44; AUC > 0.78). Multi-omics integration prioritized SPP1 as a central hub. SPP1$^+$ M2 macrophages and NETs$^+$ neutrophils preferentially localized at the tumor–stroma interface, where inferred communication converged on OPN(SPP1)–CD44/integrins and ICAM1–β2-integrin axes with downstream FAK–PI3K–Akt and NF-κB/MAPK signaling. Metabolic inference suggested a shared hypoxia/glycolysis–lactate–glutathione/antioxidant program in SPP1$^+$ M2 macrophages mirrored by NETs$^+$ neutrophils, consistent with a NETosis-permissive niche. Germline mapping indicated an antagonistic association pattern for the SPP1$^+$ M2 program. Network prioritization highlighted SRC, AKT1, and CEBPB and pathways including ECM–receptor interaction, FAK/PI3K–Akt, MAPK, and TNF/IL-17.

†Ruixiang Li, Yuheng Gu, Shi Huang and Shiya Zeng contributed equally to this work.

*Correspondence:
Mengfan Zhao
512640872@qq.com

Full list of author information is available at the end of the article

Conclusions Our framework links routine pathology morphology to NETs activity and nominates SPP1$^+$ M2 macrophages as candidate organizers of NETosis-prone high-risk niches in HCC. Importantly, the proposed macrophage–NETs axis is supported by convergent multi-omics/spatial evidence but remains primarily associative and inference-based, not definitive causation. Future work should include functional validation (e.g. macrophage–neutrophil co-culture NETosis assays, SPP1/CD44/integrin or ICAM1–ITGB2 perturbation, and in vivo depletion/blockade studies), prospective multi-center evaluation of the WSI risk score, and testing whether this axis generalizes beyond HCC or is liver-specific. These results provide a quantitative pathology-based risk stratification approach and a set of mechanistically plausible, targetable signaling–metabolic nodes for therapeutic exploration.

Keywords Hepatocellular carcinoma, NETs, SPP1$^+$ M2 macrophages, Pathology-omics

Introduction

HCC remains a leading cause of cancer burden worldwide, with marked heterogeneity, frequent recurrence, and poor prognosis despite advances in locoregional and systemic therapies [1, 2]. Beyond classical oncogenic drivers and an immunosuppressive microenvironment, NETs have been implicated in tumor cell capture/adhesion, invasion, and cancer-associated thrombosis [3, 4], underscoring an inflammatory ecology in which immunity, coagulation, and metabolism are tightly coupled.

Clinically, late-stage diagnosis and microvascular invasion or portal vein tumor thrombus markedly increase the risks of recurrence and metastasis. Current local and systemic therapies—such as TACE, ablation, and TKI/ICI combinations—provide only limited and heterogeneous benefits across patients [5]. Mechanistically, NETs can trap circulating tumor cells, initiate coagulation cascades and endothelial inflammation [6], and remodel immunosuppressive niches that enhance tumor plasticity and resistance to treatment [7]. This variability motivates biomarkers that are both prognostically informative and mechanistically interpretable from routinely available specimens such as H&E slides.

Consequently, the NETosis–adhesion/inflammation/metabolism axis represents a plausible vulnerability; however, three key gaps remain. First, the upstream cell populations and signaling programs that organize and amplify NETosis within the HCC microenvironment are not systematically defined. Second, spatial co-localization does not equate to functional interaction: proximity and ligand–receptor co-expression are inferential and may be confounded by sampling, batch effects, and cellular state heterogeneity. Third, NETosis is not directly quantifiable on routine H&E, and a unified framework linking histomorphology to molecular NETs programs and patient outcomes is lacking. Recent work in computational pathology supports that H&E morphology can encode molecular programs and prognosis [8–10], but how to anchor such signals to specific immune ecologies (e.g., NETs-permissive niches) and resolve their cellular organizers remains underdeveloped.

To address these gaps, we developed a pathology-to-single-cell multimodal pipeline.We extracted WSI features and anchored them to NETs gene-set activity to derive an interpretable pathology risk score, and then integrated scRNA-seq and spatial transcriptomics to resolve candidate organizer populations. We focused on SPP1$^+$ M2 macrophages, motivated by accumulating evidence that SPP1$^+$ tumor-associated macrophage programs expand in hypoxic lesions and shape malignant behavior across cancers [11] and in HCC [12–14]. We further inferred putative communication and metabolic coupling—including OPN(SPP1)–CD44/integrin and ICAM-1–β2-integrin adhesion axes—and evaluated whether multiple independent evidence streams (WSI, single-cell, spatial, pathway, and metabolism) converge on a consistent mechanistic model. Because our study is predominantly observational, we frame directionality (cause vs. consequence) as hypothesis-generating and highlight future perturbation experiments as necessary for causal validation.

Finally, we discuss the therapeutic implications of the nominated axes. Integrin/FAK–PI3K–Akt signaling is druggable in oncology [14, 15], and NET-targeting concepts such as DNase-based disruption have shown preclinical promise in cancer-associated thrombosis models [16]. Together, our framework provides a testable mechanistic map linking histomorphology to SPP1$^+$ M2–associated NETs-prone niches in HCC and proposes concrete future directions for functional validation and intervention.

Methods

Data sources and preprocessing

Whole-slide images (WSIs), matched bulk transcriptomic data, and clinical information for hepatocellular carcinoma (HCC) were directly sourced from the GDC Data Portal [17]. Samples were excluded if they lacked paired bulk data, survival outcomes (follow-up time or vital status), or had WSIs with low resolution or severe artifacts that compromised image quality. In total, 336 eligible samples were obtained.The NETs gene set was curated from a recently published study [18].

We analyzed GEO dataset GSE282701, which includes four HBV-negative primary tumor samples (GSM8649020, GSM8649022, GSM8649024,

GSM8649028) and one HBV-negative peritumoral sample (GSM8649029). Additionally, two primary tumor samples (GSM5076749, GSM5076750) from GSE166635 were incorporated. Spatial transcriptomics data were obtained from the CNCB/NGDC GSA-Human database (accession HRA000437) [19].

For genetic associations, summary statistics for HCC were retrieved from FinnGen R12 (phenotype C3_HEPATOCELLU_CARC; analysis set EXALLC). Cell type–level enrichment of germline risk signals was assessed using scPagwas [20].

A schematic summary of the full analytical workflow is illustrated in Fig. 1, providing an integrated view of all methodological components.

Multiscale pathology feature extraction with ResNet-50 and CellProfiler

Raw WSIs were divided into non-overlapping 512 × 512-pixel tiles [21]. To minimize inter-sample staining variability and ensure feature comparability, stain normalization was performed using the Macenko method [22]. Tiles with less than 80% tissue content were excluded to remove low-information regions.

For deep feature extraction, we applied an ImageNet-pretrained ResNet-50 (PyTorch implementation) [23]. Tiles were first normalized using ImageNet standards and then resized to 224 × 224 pixels. The resulting 2048-dimensional vector from the global average pooling layer served as the tile-level representation.

For handcrafted features, we used CellProfiler v4.2.8 [24]. Specifically, UnmixColors (optical-density deconvolution) separated the hematoxylin and eosin channels. Nuclei were segmented from the hematoxylin channel using IdentifyPrimaryObjects (size range: 5–50 pixels). Subsequently, multiscale descriptors—capturing texture, intensity, pixel distribution, and morphology—were extracted to characterize cytologic and histologic variation [24, 25].

Feature–gene-set association and feature selection

Within the aligned cohort ($n = 336$), we constructed a pathology-omics feature matrix by combining ResNet-50 deep features and CellProfiler-derived handcrafted features. We then calculated GSVA scores for a NETs-related gene set.

To prevent information leakage, only overlapping samples were included. These were randomly split into a training set ($n = 252$) and a hold-out validation set ($n = 84$) using a fixed seed (123). All feature extraction and model training were performed solely within the training set, while the validation set was reserved for independent assessment.

In the training set, we initially screened features by computing two-sided Spearman rank correlations with the NETs GSVA scores. Correlation coefficients and *p*-values were calculated, with multiple-testing correction applied using both Benjamini–Hochberg FDR and Bonferroni methods. Features that passed predefined significance thresholds constituted the "correlation candidate set."

Next, we evaluated each retained feature using univariable Cox regression for overall survival in the training set. The same procedure was applied to the validation set for consistency.

Using this filtered feature space, we built prognostic models under the Mime1 (v0.0.0.9000) framework [26]. The main evaluation metrics included time-dependent AUC and C-index, both cross-validated in training and independently assessed in validation. The final model combined stepwise Cox regression (forward selection) with a gradient boosting machine (GBM), from which feature importance and risk scores were derived for downstream analysis.

Single-cell RNA-seq processing

Single-cell data were processed using Seurat v5.0, encompassing data import, quality control, normalization, feature selection, dimensionality reduction, and clustering.

Cells were filtered according to the following criteria: 300–7000 detected genes per cell; UMI count > 1,000, with cells in the top 3% of UMI counts (per sample) excluded; mitochondrial gene percentage < 10%; and erythrocyte gene percentage < 3% [27, 28]. To further eliminate extreme outliers, cells with mitochondrial content > 20% or erythrocyte content > 5% were also removed.

Following quality control, the top 2000 highly variable genes were selected for downstream analysis.

scPagwas analysis

We applied scPagwas v2.0.0 to integrate GWAS summary statistics with single-cell RNA-seq data, aiming to uncover the genetic architecture underlying cellular differentiation and tumor progression [29]. Specifically, using the finngen_R12_C3_HEPATOCELLU_CARC_EXALLC dataset in conjunction with annotated scRNA-seq profiles, we quantified cell type–specific germline risk associations, including antagonistic (protective) signals, both across the entire dataset and within macrophage subtypes.

Pseudotime and gene-trajectory inference with Monocle3 and GeneTrajectory

We performed pseudotime analysis on macrophage subclusters using Monocle3 v1.3.7 [30]. After preprocessing with highly variable genes, we applied dimensionality reduction and learned a principal graph in UMAP space. M0 macrophages were set as the biological root, and

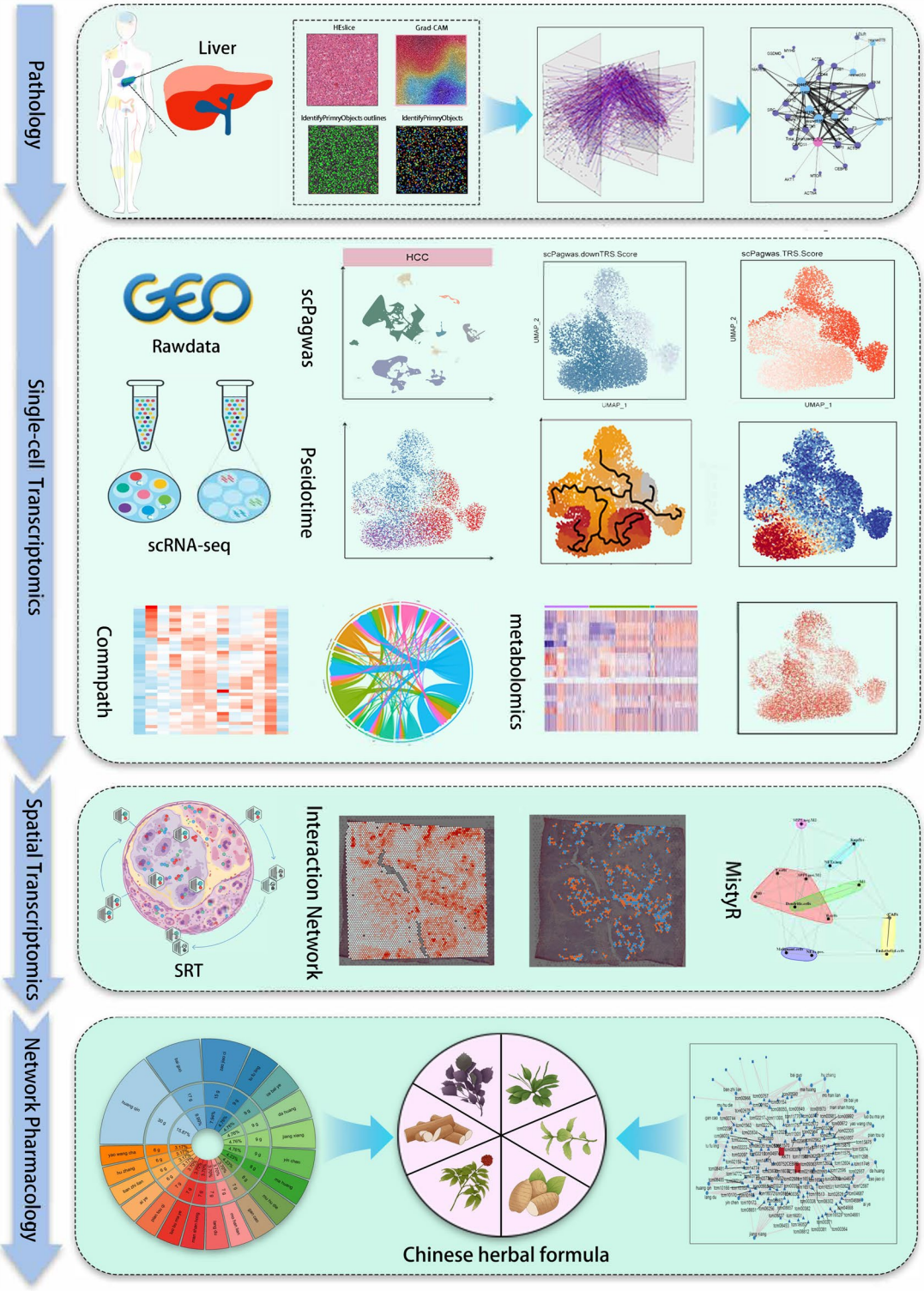

Fig. 1 Overview of analytical pipeline. schematic overview of the analytical pipeline integrating pathology image features, bulk transcriptomics, single-cell and spatial transcriptomics, and network pharmacology analyses. Pathology-based risk scores were derived from H&E whole-slide images and aligned to NETs activity (GSVA). Single-cell and spatial data were used to identify SPP1^{+} M2 macrophages and their interactions with neutrophils. Network analyses highlighted key adhesion, inflammatory, and metabolic axes converging on actionable targets

pseudotime was computed accordingly. Branch-associated genes were identified via statistical testing with FDR < 0.05.

To independently validate this trajectory, we applied GeneTrajectory v1.0.0 [19] to the same expression matrix. We first computed an optimal transport (OT) distance matrix, followed by manifold learning using Diffusion Map, and then extracted the principal trajectory (GT-time) to derive gene-level temporal dynamics across subclusters. Key NETs marker genes were projected onto the UMAP embedding to assess concordance between pseudotime and GT-time inferences.

CommPath analysis

To infer ligand–receptor (L–R) communication events, we applied CommPath v1.0.0 to the scRNA-seq dataset [31]. Cell groups containing ≥ 30 cells were designated as sender or receiver units. Genes were retained if they were expressed in at least 20% of cells in any group and had a mean expression ≥ 0.2 within that group. Based on the human L–R reference database, interaction scores were computed for all ligand–receptor pairs. Statistical significance was assessed via 10,000 permutations and adjusted using the Benjamini–Hochberg method (FDR < 0.05). Significant L–R pairs were mapped to KEGG and GO pathways, followed by pathway-level enrichment testing using the hypergeometric test with FDR correction (FDR < 0.05), yielding a functional communication network.

Inference of metabolic pathway activity with decoupleR

We used decoupleR v2.8.0 to estimate metabolic pathway activities at the single-cell level [32]. The input consisted of a Seurat-normalized expression matrix, retaining genes expressed in ≥ 10% of cells in any group with an average within-group expression ≥ 0.1. Only clusters with at least 30 cells were included in downstream analyses. Metabolic gene sets were sourced from KEGG and Reactome via msigdbr v7.5.1 (species: Homo sapiens). To ensure adequate coverage and reduce pathway sparsity, we excluded pathways containing fewer than 10 genes or with < 20% gene coverage relative to the original set.

Single-cell metabolic flux estimation with scFEA

Metabolic flux was estimated using scFEA on filtered gene expression matrices, retaining genes expressed in ≥ 10% of cells per group with a mean expression ≥ 0.1, and clusters containing ≥ 30 cells. We used the official scFEA human metabolic network [33], discarding modules with < 10 genes or < 20% effective coverage. Models were trained per sample using default parameters (seed = 123) and repeated across three seeds; median flux values were used for analysis. Quality control steps included removal of near-zero-variance modules (variance < 1e − 6), evaluation and correction of sequencing depth coupling, and inclusion of UMI count, mitochondrial percentage, and cell cycle scores as covariates. Batch and sample effects were adjusted using Harmony and/or linear mixed-effects models.

Spatial transcriptomics processing, deconvolution, and mistyR analysis

For 10x Visium data, we constructed a Seurat object and retained only on-tissue spots. We calculated mitochondrial gene percentages, removed mitochondrial/ribosomal genes and genes detected in ≤ 10 spots, and recalculated per-spot counts. High-quality spots were selected based on spatial features (nFeature_Spatial_filt > 300; nCount_Spatial_filt > 500). Data normalization was performed using SCTransform, with the SCT assay used for downstream dimensionality reduction.

Spatial deconvolution was carried out with RCTD (spacexr v2.2.1) [34], using a normalized, annotated scRNA-seq reference to estimate cell-type proportions per spot via constrained regression. Multiscale spatial dependencies were modeled with MistyR v1.10.0, incorporating both RCTD-derived cell proportions and proportion-weighted gene expression profiles. Three spatial views were defined: intra-spot (local), juxta-spot (neighbor mean, ~50–100 μm), and para-spot (ring mean, ~100–200 μm).

Network analysis from gene set to prescriptions with TCMNP

We performed network pharmacology using TCMNP v0.1.0, with the NETs gene set as disease targets. Targets were standardized to HGNC symbols [35], and highly promiscuous proteins (degree > 95th percentile) were removed to reduce network bias. Herb/compound–target associations were evaluated using tcm_prescription via hypergeometric enrichment. p values were adjusted using Benjamini–Hochberg correction (FDR < 0.05).

We calculated two prioritization metrics: richFactor (hit targets/annotated targets) and a composite score ($-\log_{10}$(FDR) × richFactor). Significant items were assembled into Herb–Compound–Target networks. Centrality metrics—including degree, betweenness, and PageRank—were computed to identify key nodes. Target genes were further subjected to KEGG and GO enrichment analysis (q < 0.05) to infer potential mechanisms of action.

Statistical analysis and data handling

Statistical analyses and visualizations were performed using R v4.3.3. Correlations between continuous variables were evaluated using Spearman's method, while categorical comparisons were made using the χ^2 test. Group differences were assessed with either the Wilcoxon

rank-sum test or Student's/Welch's t-test, depending on the distributional assumptions of the data.

For high-dimensional analyses, such as gene, pathway, or module testing, multiple comparisons were corrected using the Benjamini–Hochberg procedure (FDR < 0.05). In cases where empirical null distributions were required, such as for network, spatial, or pathway activity models, significance was determined by label permutation or spatial rewiring (n = 10,000), followed by Benjamini–Hochberg correction.

Longitudinal trends along pseudotime or GT-time were examined using Cuzick's trend test or generalized additive models (GAMs).Unless otherwise specified, all statistical tests were two-sided with significance defined as $p < 0.05$ or FDR < 0.05. All random operations were performed with a fixed seed (set.seed(123)) to ensure reproducibility.

Results

Construction and validation of a pathology-omics–based NETs prognostic risk score

We constructed a pathology-omics–based risk score by integrating handcrafted and deep features extracted from diagnostic whole-slide images (WSIs). TCGA cases (n = 336) were randomly split into a training set (n = 252) and a hold-out validation set (n = 84) using a 75%/25% split, a commonly adopted ratio that ensures sufficient sample size for model construction while retaining an independent dataset for unbiased performance evaluation. NETs activity was quantified using GSVA on matched bulk RNA-seq profiles.

In the training set, we computed Spearman correlations between features and NETs GSVA scores, applying an FDR threshold of < 0.05. Significant associations were visualized (Fig. 2A). Next, z-scored features were tested using univariable Cox regression for overall survival (Fig. 2B). Several deep features were associated with worse prognosis (HR > 1; 95% CI excluding 1), while *Total_Granularity_1–Hematoxylin*, a handcrafted feature, showed a protective effect (HR < 1). These variables were retained as candidates for multivariable modeling.

Using the Mime1 framework, we evaluated 101 machine learning models via cross-validation. Tree-based and Cox-type models demonstrated the highest stability. A combined stepwise Cox regression (forward selection) and gradient boosting machine (GBM) achieved optimal discrimination with minimal overfitting and was selected for downstream analysis (Fig. 2C).

Risk scores from the final model, dichotomized at the median, produced clear Kaplan–Meier separations in both training (HR ≈ 8.48) and validation cohorts (HR ≈ 6.44; both $p < 0.001$; Fig. 2D–E). Time-dependent ROC curves showed high predictive performance, with AUCs > 0.78 at 1, 3, and 5 years in both sets (Fig. 2F–H).

In multivariable Cox regression models including age, sex, stage, and risk score, both stage and the pathology-omics risk score emerged as independent prognostic factors. The risk score remained significant in a reduced model excluding other covariates (Fig. 2I–J).

Reanalysis of FDR-adjusted NETs correlations among candidate features revealed that most deep features were positively associated with NETs GSVA scores, whereas the handcrafted feature showed a negative correlation (Fig. 2K). A unified network integrating deep, handcrafted, and transcriptomic NETs signals identified central hubs, including *SPP1* (Fig. 2 L). Stratification by *SPP1* expression revealed significantly worse survival in the high-expression group (Fig. 2 M).

Single-cell atlas and scPagwas reveal antagonistic germline association in SPP1$^+$ M2 macrophages

Following stringent quality control, we used canonical marker genes to annotate major cellular lineages. UMAP embeddings revealed eight principal cell types within the tumor and its microenvironment: B cells, T cells, dendritic cells, endothelial cells, cancer-associated fibroblasts (CAFs), macrophages, neutrophils, and malignant epithelial cells (Fig. 3A). Cluster-level expression heatmaps and pathway enrichment analysis (Fig. 3B) confirmed lineage-appropriate biological programs, including immune responses, angiogenesis, neutrophil chemotaxis, and epithelial polarity and adhesion.

We next focused on the hub gene *SPP1*, whose expression was highly cell type–specific and strongly enriched in macrophages (Fig. 3C). To explore the genetic underpinnings of this distribution, we applied *scPagwas* across all single cells to estimate polygenic burden at single-cell resolution. Based on gPAS and TRS scores, malignant epithelial cells exhibited the highest germline susceptibility, whereas multiple immune lineages—notably macrophages—displayed broadly antagonistic associations with germline risk (Figs. 3D–F). This suggests that tumor cells more directly reflect inherited and somatic oncogenic signals, while immune cell states are largely shaped by paracrine or environmental cues.

To further resolve the myeloid compartment underlying *SPP1* biology, we performed a two-stage stratification within macrophages (Fig. 3 G). Kupffer cells were identified by canonical markers (*CLEC4F, MARCO, VSIG4*), and monocyte-derived macrophages (MDMs) by *FCN1, LST1, S100A8/S100A9*. Within MDMs, cells were stratified into M0, M1, and M2 subsets based on polarization markers. M2 cells were further divided by *SPP1* expression into *SPP1$^+$ M2* and *SPP1$^-$ M2* subsets (threshold: *SPP1* > 0).

Applying *scPagwas* to these macrophage subtypes (M0, M1, *SPP1$^+$ M2*, *SPP1$^-$ M2*) revealed that M0 cells retained relatively stronger germline association, while

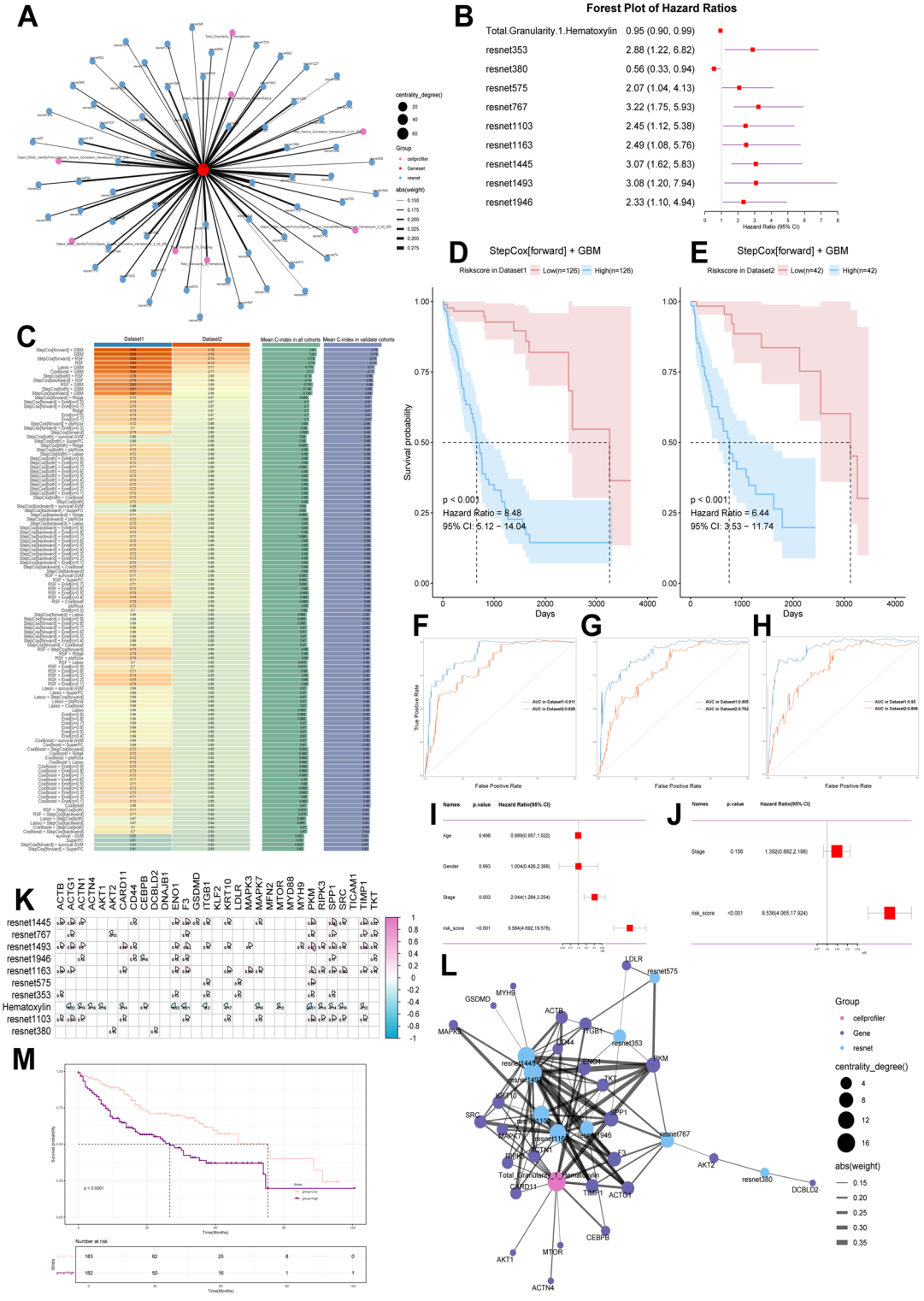

Fig. 2 Construction and validation of a pathology-omics–based NETs risk score. (**A**) Spearman correlations between pathology features and NETs GSVA (FDR < 0.05); node size = centrality, edge width = correlation. (**B**) univariable Cox (z-scored features); deep features predict poor outcome (HR > 1), hand-crafted feature is protective (HR < 1). (**C**) model cross-validation within Mime1; stepwise Cox + GBM selected for low overfitting. (**D**–**E**) Kaplan–meier curves by median risk score: clear separation in training and validation. (**F**–**H**) ROC at 1/3/5 years: AUC > 0.78. (**I**–**J**) multivariable Cox shows stage and risk score are independent predictors. (**K**) Spearman correlations between candidate features and NETs gene set. (**L**) integrated network highlighting SPP1 as a hub. (**M**) survival by SPP1 expression

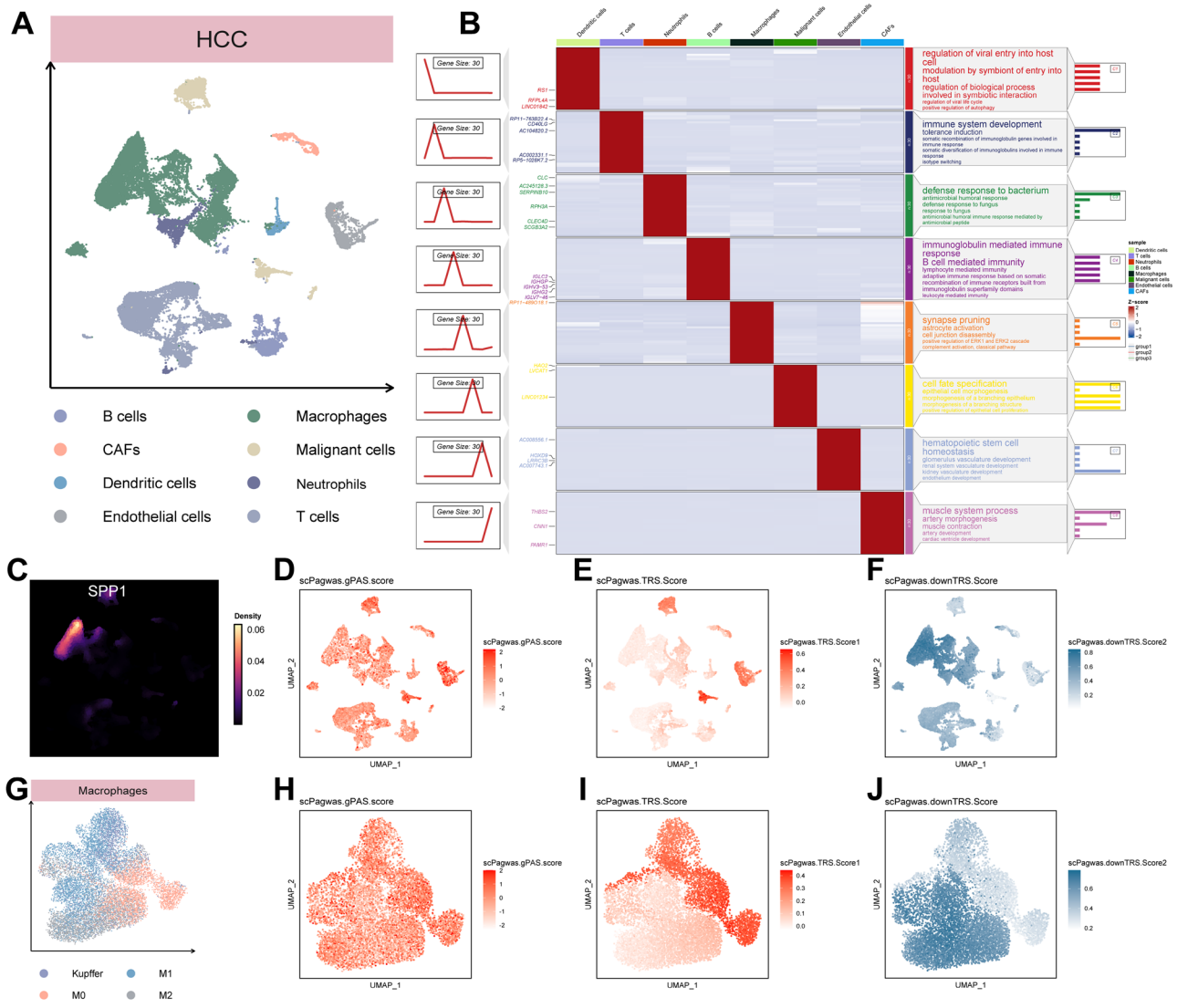

Fig. 3 Single-cell mapping of SPP1$^+$ M2 and germline association. (**A**) UMAP of 26,928 cells showing eight major lineages. (**B**) Heatmap and enrichment pathways per cluster. (**C**) SPP1 expression concentrated in macrophages. (**D**–**F**) scPagwas shows gPAS peak in tumor cells, antagonistic (downTRS) signals in immune lineages. (**G**) macrophages subdivided into Kupffer and MDM; MDM into M0/M1/M2. (**H**–**J**) within macrophages: M0 shows strongest gPAS; SPP1$^+$ M2 shows strongest downTrs

SPP1$^+$ *M2* macrophages demonstrated the most pronounced antagonistic signal (Fig. 3H–J). This finding aligns with the immunosuppressive and tissue-remodeling phenotype of *SPP1*$^+$ *M2* cells and supports the hypothesis that their activation state is primarily driven by microenvironmental instruction rather than germline predisposition.

Monocle3–GeneTrajectory concordance defines a single MDM polarization axis

Within the monocyte-derived macrophage (MDM) compartment, single-cell visualization revealed marked heterogeneity in *SPP1* expression (Fig. 4A). Preserving the canonical M0/M1/M2 functional stratification, we further subdivided M2 cells based on *SPP1* expression into *SPP1*$^+$ *M2* and *SPP1*$^-$ *M2* subsets, using a threshold of *SPP1* > 0.

To explore dynamic transitions among macrophage states, we conducted pseudotime analysis using *Monocle3*, with root assignment to the M0-enriched region. The inferred trajectory showed a progressive increase in pseudotime from M0 toward M2, terminating in a region enriched for *SPP1*$^+$ *M2* cells (Fig. 4B–C).

To independently validate this progression, we applied *GeneTrajectory* inference based on diffusion map geometry. The analysis recovered a single principal trajectory (Fig. 4D), indicating that MDMs in this dataset follow a dominant linear polarization axis.

We divided this trajectory into five equidistant bins (localBin1–5) to assess dynamic changes in gene

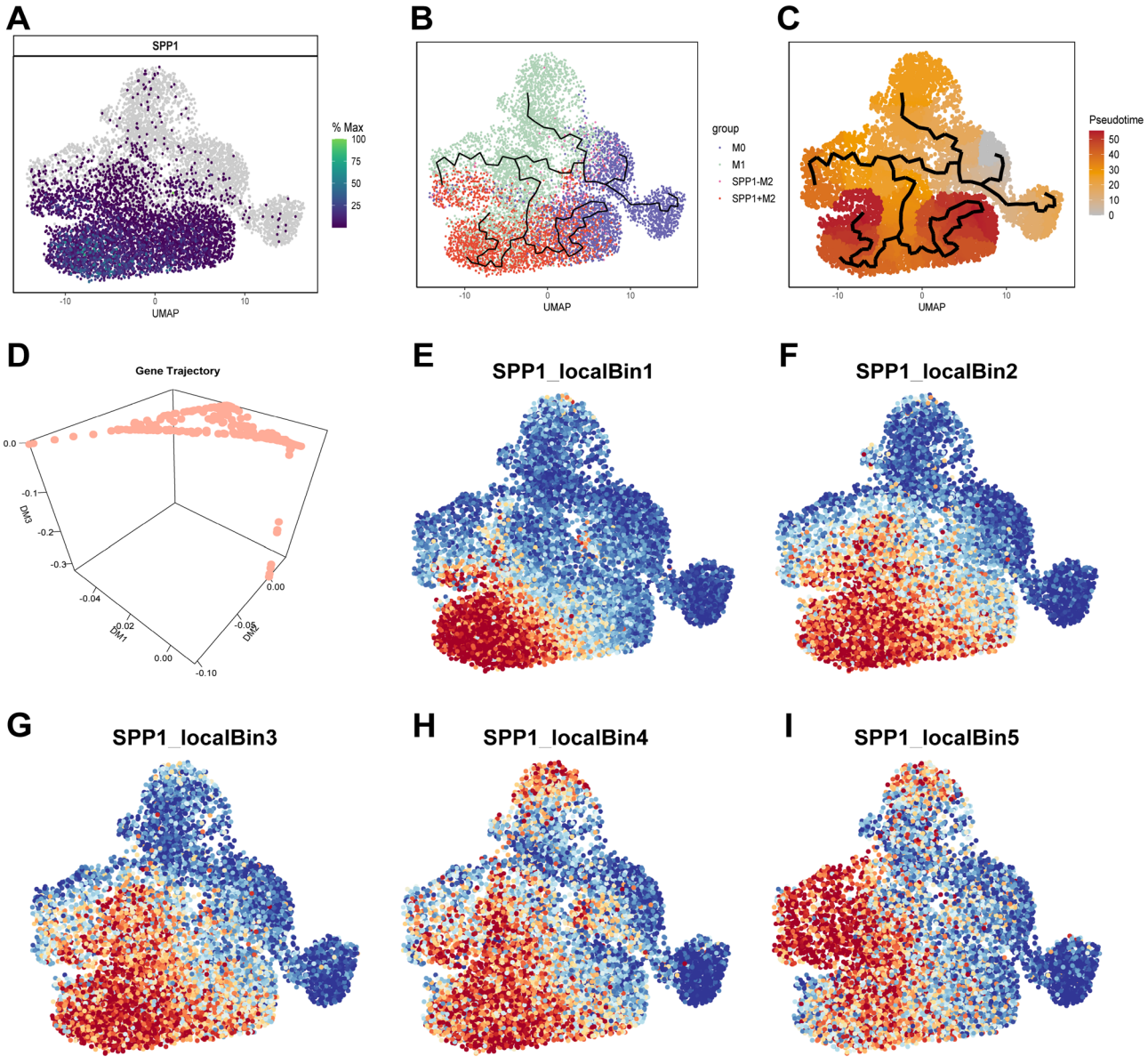

Fig. 4 SPP1 increases along macrophage pseudotime trajectory. (**A**) SPP1 expression in MDM. (**B**–**C**) Monocle3 pseudotime from M0 to SPP1$^+$ M2. (**D**) GeneTrajectory confirms a single trajectory. (**E**–**I**) SPP1 increases from localBin1 to Bin5, peaking in late segments

expression. *SPP1* expression increased monotonically along the pseudotemporal axis and peaked in the terminal segments (Fig. 4E–I).

Taken together, these findings consistently support the presence of a continuous MDM polarization trajectory, with *SPP1* upregulation marking a terminal, immunosuppressive activation state corresponding to *SPP1*$^+$ *M2* macrophages.

A SPP1$^+$ M2–NETs$^+$ neutrophil–centered communication network and pathway cascades

To embed macrophage subclusters and neutrophil NETs phenotypes within a unified communication framework, we stratified neutrophils into *NETs-positive* and *NETs-negative* subsets based on a NETs-related gene signature. These labels were projected back onto the single-cell atlas and analyzed using *CommPath* to quantify cell–cell interactions (Fig. 5A).

At the pathway level, *SPP1*$^+$ *M2* macrophages exhibited high activity across a broad spectrum of signaling categories, including extracellular matrix remodeling, cytoskeletal organization, angiogenesis, inflammatory signaling, and innate immune functions such as phagocytosis (Fig. 5B). These profiles point to a composite phenotype involved in matrix dynamics, chemotaxis, and immune modulation. Communication intensity was particularly elevated between *SPP1*$^+$ *M2* and malignant epithelial cells, CAFs, endothelial cells, and *NETs-positive*

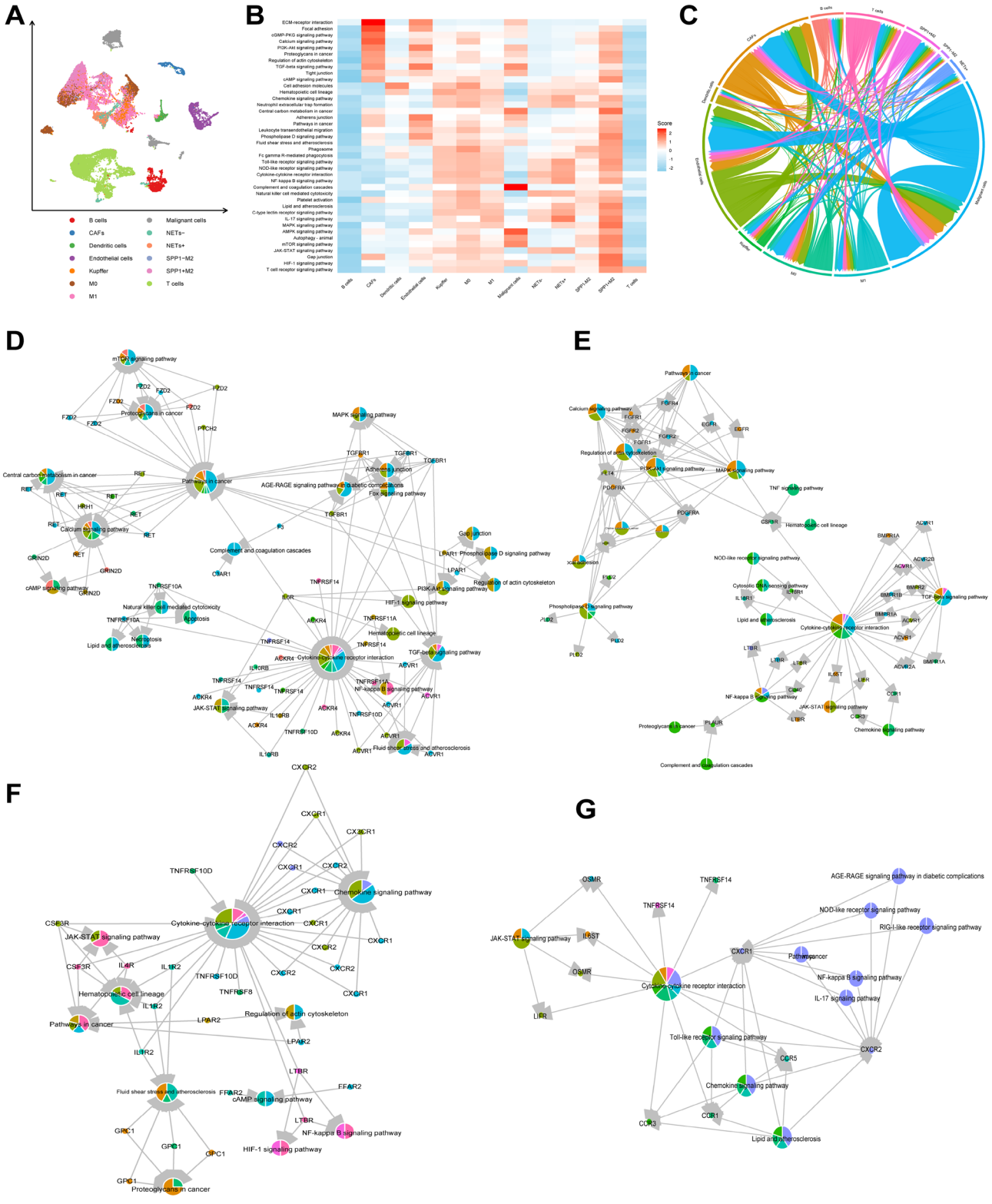

Fig. 5 Communication network between SPP1^{+} M2 and NETs^{+} neutrophils. (**A**) Refined labels projected to UMAP. (**B**) CommPath: SPP1^{+} M2 enriched in adhesion, chemotaxis, immune signaling. (**C**) chord diagram shows SPP1^{+} M2 connects strongly with tumor, endothelium, CAFs, and NETs^{+}. (**D**–**E**) ligand–receptor–pathway mapping from SPP1^{+} M2. (**F**–**G**) analogous analysis for NETs^{+} neutrophils: key inflammatory and adhesion pathways identified

neutrophils (Fig. 5C), highlighting *SPP1*$^+$ *M2* as a key node in the multicellular crosstalk network.

We next dissected ligand–receptor interactions emanating from *SPP1*$^+$ *M2* macrophages (Fig. 5D). A dominant adhesion axis was observed, involving osteopontin (encoded by *SPP1*) engaging CD44 and multiple integrin complexes, including those with ITGAV and ITGB1/3/5. Additional signaling routes included transforming growth factor beta (TGF-β), CCL-family chemokines such as CCL2 and CCL5 acting on CCR2/CCR5, and vascular endothelial growth factor (VEGF) targeting canonical VEGF receptors. These interactions converged on downstream programs involving ECM–receptor engagement, focal adhesion signaling, PI3K–Akt activation, TGF-β modulation, and chemokine pathways (Fig. 5E).

Parallel analysis of *NETs-positive* neutrophils revealed complementary signaling modules (Fig. 5F–G). Chemokine signaling was driven by CXCL8 and CXCL2 engaging CXCR1 and CXCR2. Inflammatory signals prominently featured TNF and IL1B, acting through their respective receptor families. Adhesion signaling was mediated via ICAM1 in combination with integrin binding. These upstream cues connected to downstream networks involving NF-κB and MAPK cascades, NOD-like receptor signaling, and migration-related adhesion pathways—molecular signatures consistent with inflammatory amplification and immune remodeling during NETosis.

Finally, a receptor-centric network centered on *SPP1*$^+$ *M2* macrophages (Fig. 6A) showed that tumor cells, CAFs, endothelial cells, and dendritic cells serve as key upstream signal providers. These inputs funneled into functional programs such as phagosome formation and HIF-1 signaling, indicative of phagocytic activation and hypoxic stress adaptation. Notably, lipid metabolic and mechanotransduction-related pathways—such as those associated with atherosclerosis and fluid shear stress—were also prominent, suggesting that *SPP1*$^+$ *M2* cells respond to dynamic mechanical and metabolic cues in the tumor microenvironment.

NF-κB–Driven metabolic rewiring in SPP1$^+$ M2 macrophages shapes a pro–NETosis microenvironment

We quantified pathway-level activity across macrophage subpopulations using decoupleR and visualized z-scored gene-set scores (Fig. 6B). Among all subgroups, *SPP1*$^+$ *M2* macrophages showed markedly elevated activity across inflammatory and stress-related signaling modules, including tumor necrosis factor signaling and nuclear factor kappa B (NF-κB) activation. They also demonstrated upregulation in hypoxia-associated and glycolytic programs. In contrast, M0 and M1 subsets showed lower overall activity. A representative spatial projection of the TNF–NF-κB signature (HALLMARK_TNFA_SIGNALING_VIA_NFKB; Fig. 6C) displayed a spatially continuous high-expression domain that was confined to the monocyte-derived macrophage population, reinforcing the interpretation that *SPP1*$^+$ *M2* exhibit an activated, NF-κB–dominated inflammatory state.

To further explore metabolic alterations, we applied scFEA to estimate reaction-level fluxes at single-cell resolution. *SPP1*$^+$ *M2* macrophages showed upregulated flux across a range of key biochemical processes (Fig. 6D), particularly in glycolysis, redox buffering, and purine degradation. Distribution plots (Fig. 6E) demonstrated a rightward shift in flux intensity in the *SPP1*$^+$ *M2* group, with clear separation from other macrophage states. Heatmaps (Fig. 6F) further highlighted a discrete band of elevated metabolic activity, distinguishing *SPP1*$^+$ *M2* from M0, M1, and *SPP1*$^-$ *M2* subtypes. These patterns are consistent with a reprogramming signature characterized by lactate generation and glutathione biosynthesis—key features of an antioxidant-adapted macrophage phenotype.

We next asked whether neutrophil metabolism parallels NETosis status. Using the NETs gene-set score, we stratified neutrophils into *NETs-positive* and *NETs-negative* states and assessed their metabolic flux profiles (Fig. 6 G–I). Compared with their NETs$^-$ counterparts, *NETs-positive* neutrophils exhibited higher flux through glycolytic and antioxidant pathways—mirroring the metabolic profile of *SPP1*$^+$ *M2* macrophages. This alignment suggests a reciprocal relationship: NETs-forming neutrophils may rely on lactate-rich, redox-favorable niches, while *SPP1*$^+$ *M2* macrophages establish such environments by enhancing glycolysis and antioxidant output. Together, these findings support a model of metabolic cooperation that reinforces NETosis within the tumor microenvironment.

Spatial transcriptomics: SPP1$^+$ M2 enrichment and multiscale interactions

Following rigorous quality control of spatial transcriptomics data, we applied RCTD to integrate single-cell annotations with spatial spots. The resulting cell-type compositions included Kupffer cells, M0/M1/SPP1$^-$/SPP1$^+$ M2 macrophages, malignant epithelial cells, endothelial cells, CAFs, B and T cells, as well as *NETs-positive* and *NETs-negative* neutrophils. Spatial abundance maps revealed a band-like accumulation of *SPP1*$^+$ *M2* macrophages along the tumor–stroma interface (Fig. 7A).

To investigate local cellular dependencies, we constructed a three-scale multiview spatial model using *mistyR*. The three views captured intra-spot (intra), near-neighbor (juxta_5), and broader-ring (para_15) relationships. Model results showed that *SPP1*$^+$ *M2* was among the most neighborhood-predictable cell types, with

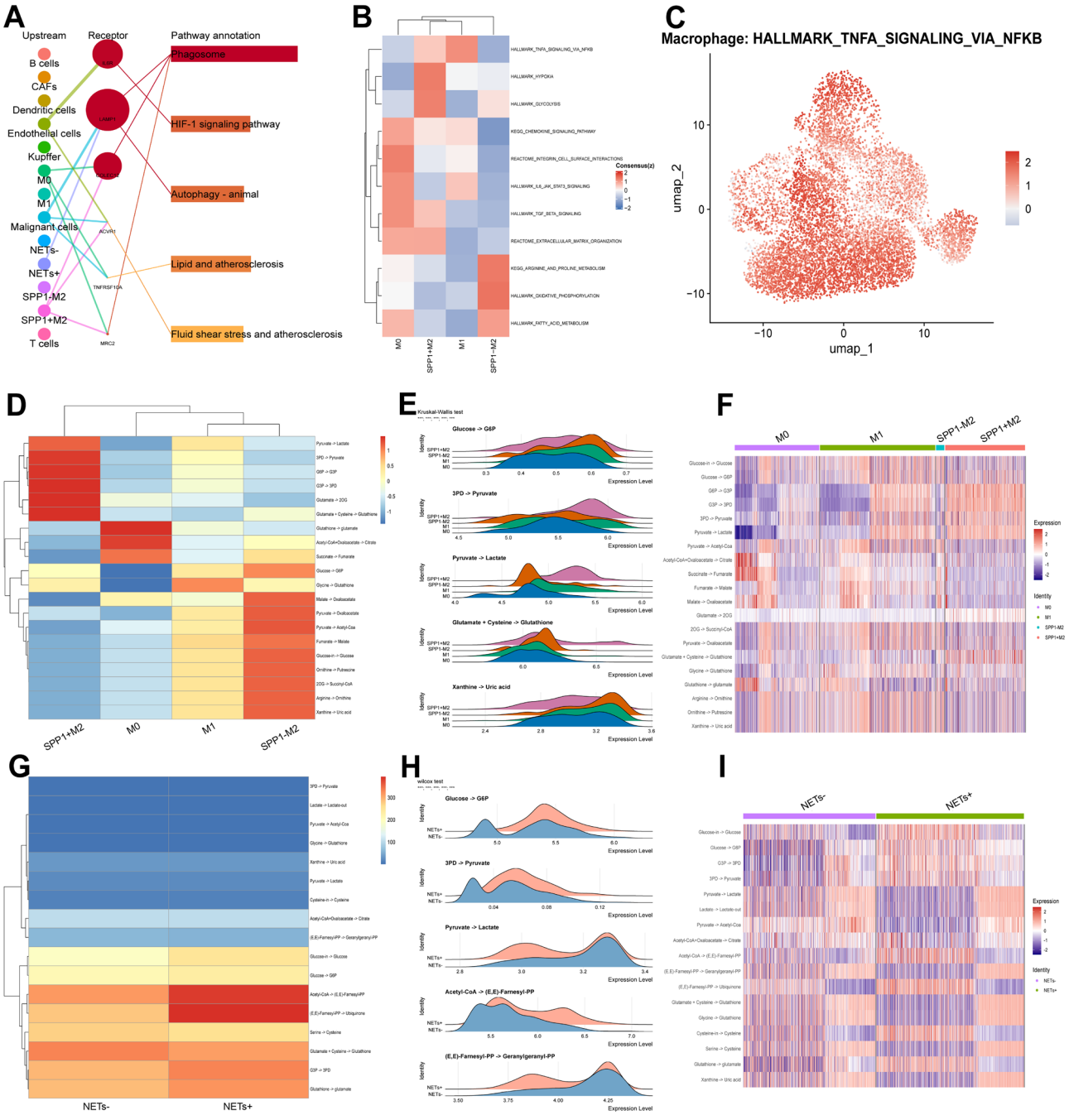

Fig. 6 Metabolic reprogramming in SPP1$^+$ M2 and NETs$^+$ neutrophils. (**A**) L–R network centered on SPP1$^+$ M2. (**B**) decoupleR: SPP1$^+$ M2 high on NF-κB, glycolysis, hypoxia axes. (**C**) TNFA/NF-κB expression localized to SPP1$^+$ M2. (**D**–**F**) scFEA shows elevated glycolysis, GSH synthesis, and purine metabolism in SPP1$^+$ M2. (**G**–**I**) NETs$^+$ neutrophils show similar flux patterns

explained variance dominated by intra and juxta_5 scales (Fig. 7B–C).

At the intra-spot level (Fig. 7D–E), *SPP1$^+$ M2* abundance strongly co-occurred with malignant epithelial cells, CAFs, and *NETs-positive* neutrophils. This pattern suggests co-localized adhesion and inflammatory cues within the same microenvironmental unit. At the juxta_5 scale (Fig. 7F–G), short-range coupling intensified between *SPP1$^+$ M2* and malignant epithelium or *NETs-positive* neutrophils, and new interactions emerged with Kupffer and M1 macrophages. At the para_15 scale (Fig. 7H–I), longer-range spatial associations appeared between *SPP1$^+$ M2* and T cells, indicating potential adaptive immune influences on macrophage polarization beyond the immediate niche.

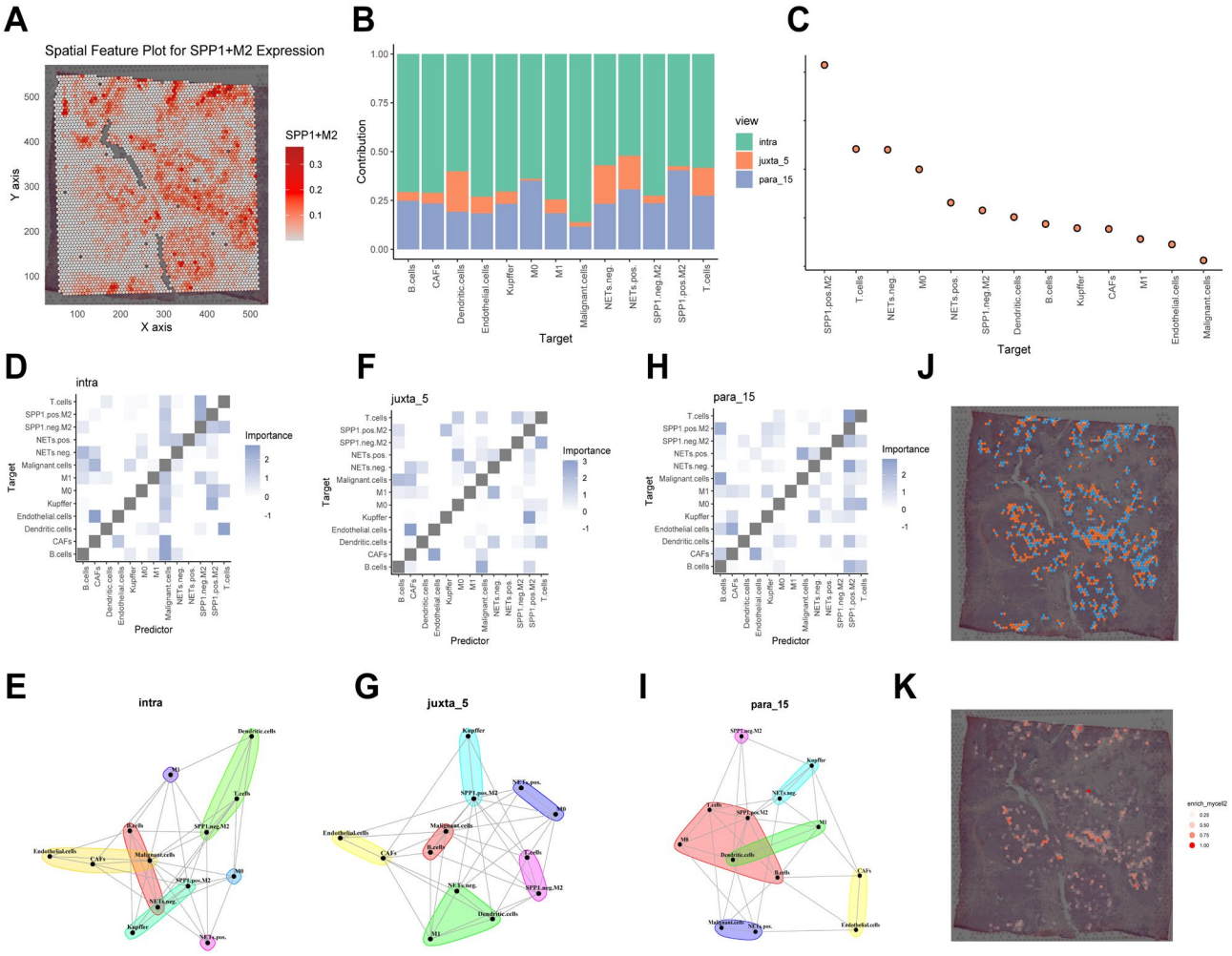

Fig. 7 Spatial localization and neighborhood interactions. (**A**) RCTD deconvolution: SPP1$^+$ M2 enriched at tumor–stroma interface. (**B**–**C**) variance explained across intra/juxta/para scales; SPP1$^+$ M2 highly predictable. (**D**–**I**) neighborhood-level interactions with tumor, CAFs, NETs$^+$ neutrophils, T cells. (**J**–**K**) heterotypic SPP1$^+$ M2–NETs$^+$ network: spatial projection and enrichment

To formally evaluate spatial co-occurrence between *SPP1$^+$ M2* and *NETs-positive* neutrophils, we constructed a heterotypic interaction network. An edge was defined when a central spot had > 50% *SPP1$^+$ M2* content and its adjacent region had > 30% *NETs-positive* neutrophils. These cell pairs consistently formed stable spatial clusters across tissue slices (Fig. 7J), with slice-level enrichment visualized in Fig. 7K.

Taken together, these findings position *SPP1$^+$ M2* macrophages at the center of a tumor–stroma–inflammatory axis. Their state is strongly shaped by neighboring cell types and local microenvironments. Moreover, the spatial coupling between *SPP1$^+$ M2* and *NETs-positive* neutrophils supports a model in which matrix remodeling and inflammatory amplification jointly stabilize pro-tumor NETosis niches.

Construction of TCM prescriptions and analysis of the hit target gene set

Using the NETs gene set as the input disease signature, we applied tcm_prescription to identify candidate herbal formulations. Hypergeometric enrichment was conducted with Benjamini–Hochberg correction (FDR < 0.05), and prescriptions were prioritized using a composite score: the negative logarithm of the FDR multiplied by the richFactor. This yielded a panel of high-ranking herbs, including *Tinglizi* (Semen Lepidii), *Huzhang* (Polygonum cuspidatum), *Qinghao* (Artemisia annua), *Kuxingren* (Semen Armeniacae amarum), *Mabiancao* (Verbena officinalis), *Gancao* (Glycyrrhiza spp.), *Mahuang* (Ephedra spp.), and *Guanghuoxiang* (Pogostemon cablin).

To refine functional interpretation, we filtered the NETs gene set to retain only those targets mapped to at least one selected prescription. This subset of "hit targets" was used for downstream enrichment and network

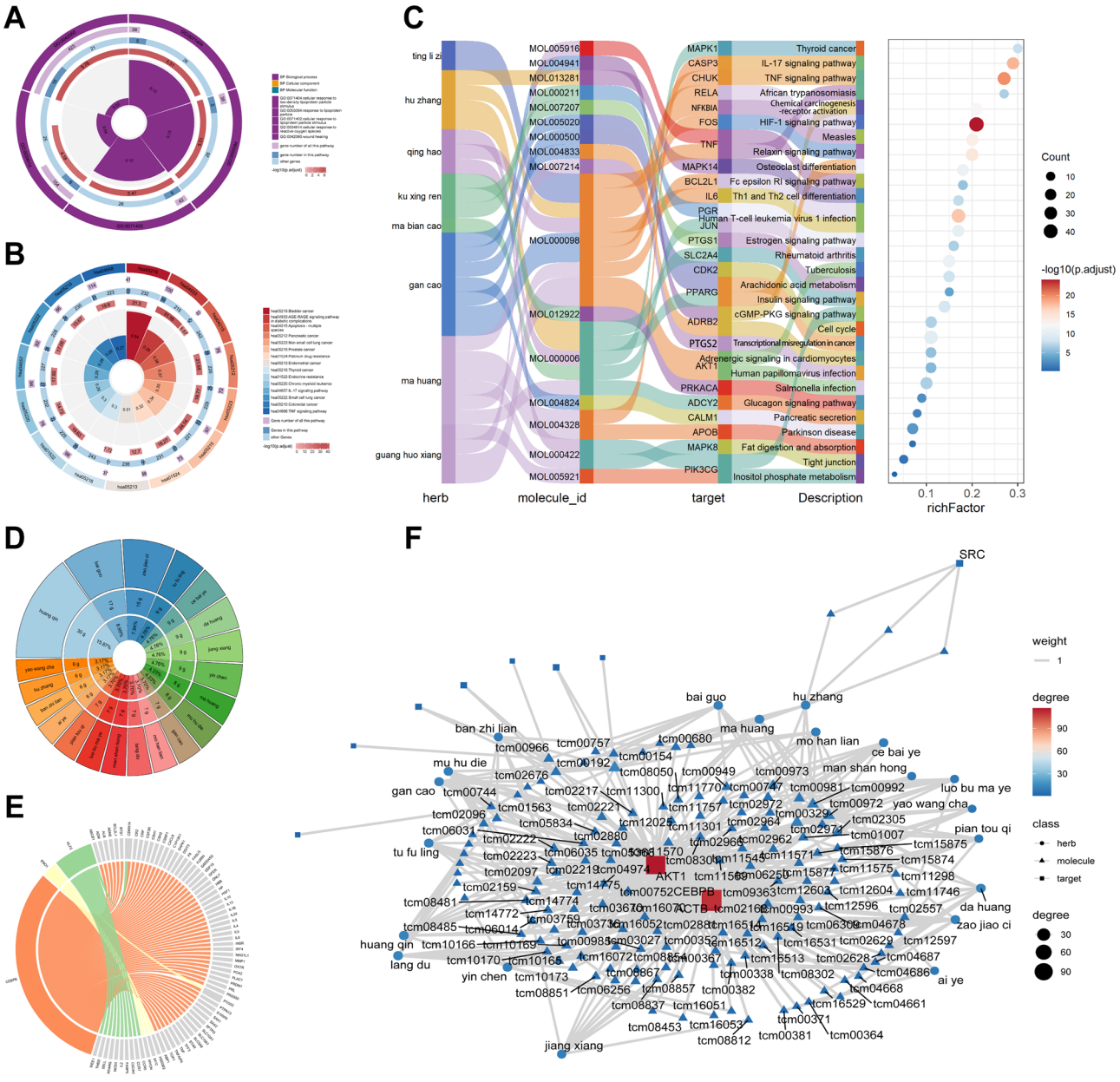

Fig. 8 NETs-targeted TCM prescriptions and mechanistic links. (**A**–**B**) GO and KEGG enrichment of hit-targets. (**C**) Sankey diagram: drug → ingredient → target → Pathway. (**D**–**E**) Herb properties and pathway alignment: predominance of cold/bitter herbs and liver/spleen targeting. (**F**) Drug–ingredient–target network showing SRC, AKT1, CEBPB as hubs in inflammation and adhesion pathways

construction. Gene Ontology (GO) analysis (Fig. 8A) highlighted biological processes related to wound healing, oxidative stress response, and regulation of inflammation. Cellular component enrichment pointed to extracellular matrix structures and adhesion-related elements, while molecular functions included cytokine receptor and integrin binding, as well as kinase regulation.

Pathway-level insights from KEGG (Fig. 8B) revealed activation of ECM–receptor interaction, focal adhesion, actin cytoskeleton regulation, PI3K–Akt and MAPK signaling, IL-17 and TNF pathways, complement/coagulation cascades, and leukocyte migration. These results converge on a composite mechanism involving matrix remodeling, immune–inflammatory modulation, and survival signaling—aligned with pathways implicated in tumor progression and therapy resistance.

To bridge herbal composition and functional effects, we constructed a four-layer network linking drugs, active ingredients, molecular targets, and downstream pathways (Fig. 8C). Network centrality analysis (Fig. 8F)

identified *SRC*, *AKT1*, and *CEBPB* as high-betweenness hubs coordinating multiple key axes.

Moreover, TCM property annotation revealed a dominance of herbs with "cold" and "bitter" attributes, and meridian association primarily with the liver and spleen (Fig. 8D). This profile aligns with traditional therapeutic principles such as "heat-clearing and detoxification" and "spleen harmonization with dampness resolution." A property–mechanism chord diagram (Fig. 8E) further illustrated co-occurrence patterns between frequently co-used herb pairs and core biological modules.

Discussion

Within the tumor microenvironment, tumor-derived G-CSF and extracellular vesicles can prime neutrophils, enhancing their propensity to undergo NETosis [36–38]. Upon activation, neutrophils generate reactive oxygen species (ROS) via NADPH oxidase, initiating PAD4-mediated histone citrullination and chromatin decondensation [39, 40]This cascade culminates in the rupture of nuclear and granule membranes, releasing extracellular DNA webs decorated with granule enzymes—collectively known as NETs [41, 42].

NETs exert multifaceted pro-tumorigenic effects. For instance, NET-associated enzymes such as neutrophil elastase (NE) and MMP9 remodel the extracellular matrix, modifying laminin structures and activating α3β1 integrin signaling, which can awaken dormant tumor cells and promote recurrence. NET-derived DNA can be sensed by the tumor-cell surface receptor CCDC25 [43], triggering the ILK–β-parvin signaling cascade to enhance cell migration and metastatic dissemination [44]. In addition, the NET scaffold impedes the infiltration of effector lymphocytes and contributes to T cell exhaustion [7, 45], facilitating the formation of an immunosuppressive niche. In circulation, NETs serve as scaffolds for coagulation and platelet adhesion, thereby linking cancer-associated thrombosis with metastatic progression [46, 47].

Interestingly, recent studies have also highlighted PAD4-independent pathways of NETosis, particularly those driven by mitochondrial ROS. These observations point to the idea that NET formation occurs within a context-dependent threshold. Such a threshold is likely influenced by a combination of metabolic and inflammatory signals present in the surrounding microenvironment.

SPP1 encodes osteopontin (OPN), a secreted phosphoglycoprotein that engages CD44 and a range of integrins—including α_vβ$_3$, α_vβ$_5$, $\alpha_4\beta_1$, and $\alpha_9\beta_1$—to initiate intracellular signaling cascades. These interactions activate FAK–PI3K–Akt and NF-κB/MAPK pathways, thereby promoting epithelial–mesenchymal transition (EMT), invasion, angiogenesis, and enhanced glycolysis in tumor cells [48–50]. Notably, cleavage of OPN by thrombin exposes the SVVYGLR motif, which selectively binds $\alpha_4\beta_1$ and $\alpha_9\beta_1$ integrins, further amplifying inflammatory adhesion and migratory programs within the tumor microenvironment.

While much of this literature has centered on tumor-intrinsic effects, our findings suggest that SPP1$^+$ macrophages may hijack similar adhesion and signaling modules to coordinate inflammation, matrix remodeling, and metabolic adaptation. This expands the functional relevance of the OPN axis from tumor cells to key immune subsets that structure the tumor–stroma interface.

By integrating pathology imaging, single-cell resolution data, spatial deconvolution, cell–cell communication, and metabolic-flux modeling within a unified framework, our study identifies an SPP1$^+$ M2 macrophage–orchestrated microenvironment that is tightly associated with NETosis in HCC. Importantly, the evidence presented here is primarily correlative, and therefore does not, by itself, prove direct causality. Nevertheless, multiple independent evidence streams (pathology-derived risk features, single-cell state programs, spatial co-localization, ligand–receptor inference, and metabolic-flux convergence) collectively support a coherent mechanistic model in which a macrophage-organized niche lowers the NETosis threshold and maintains its spatial persistence.

Importantly, deep image features emerged as strong adverse prognostic markers not simply due to increased immune-cell infiltration, but because they captured nuanced morphological changes—such as texture coarsening, stromal boundary disruption, and fibrotic remodeling—at the tumor–stroma interface. These macro-morphological patterns are biologically plausible readouts of NET-associated processes. NETs can promote **microvascular occlusion and immunothrombosis** (which can manifest histologically as microthrombi, ischemic injury, and interface disruption) [47], and NET-derived components can drive **fibroblast activation and collagen production**, providing a mechanistic bridge to stromal remodeling and coarse texture patterns [51]. Consistently, collagen architecture and stromal remodeling can be quantified from routine histopathology and are known to shape texture/boundary features in digital pathology analyses [52]. Thus, image-derived features offer a macroscopic signature of a NETosis-prone and pro-thrombotic tumor ecology.

In contrast, the classic handcrafted granularity feature, which was associated with better prognosis, likely reflects preserved nuclear structure and minimal necro-inflammation—traits inversely correlated with histological NETosis. This convergence of morphological and molecular signals may explain the ability of whole-slide imaging–based risk scores to stratify outcomes even across visually similar H&E slides.

Within the monocyte-derived macrophage lineage, both Monocle3 and GeneTrajectory consistently revealed a single polarization trajectory from M0 to SPP1$^+$ M2, with a gradual increase in SPP1 expression along pseudotime.The gene set we have constructed to capture the NETs-related processes reflects the dynamic nature of NET formation. Notably, the progressive emergence of the SPP1$^+$ M2 state, which occurs upstream of the NETs-high ecology, lends weight to a specific hypothesis: the polarization of SPP1$^+$ M2 is likely more integral to initiating and organizing conditions conducive to NET formation, rather than merely acting as a downstream consequence. This suggests that SPP1$^+$ M2 polarization may play a crucial role in the sequence leading to NET formation. Our trajectory and spatial analyses support this model, indicating that SPP1$^+$ M2 polarization might not simply follow but rather precede and actively facilitate NET formation. However, while these observations are compelling, the establishment of a definitive causal link will still require further functional perturbation experiments.

At the communication level, SPP1 (osteopontin) secreted by SPP1$^+$ M2 binds CD44 and integrins such as αvβ3, α4β1, and α9β1, thereby activating adhesion-associated FAK–PI3K–Akt and inflammatory NF-κB/MAPK cascades [48]. In parallel, ICAM-1, expressed on stromal and endothelial surfaces, interacts with β2-integrins (LFA-1 and Mac-1) on neutrophils, increasing neutrophil arrest, dwell time, and transendothelial migration [53, 54]. These dual axes reinforce adhesion and inflammation, creating a microenvironment that facilitates sustained neutrophil recruitment and activation.

Tumor cells, endothelial cells, and CAFs cooperate with SPP1$^+$ M2 by secreting CXCL8, TNF, IL-1, CCL2, CCL5, TGFB1, and VEGFA. These ligands engage their respective receptors—CXCR1/2, TNFR, IL-1 R, CCR2/5, TGFBR, and FLT1—to amplify chemotaxis, pro-inflammatory signaling, and adhesion, thus lowering the activation threshold for NETosis [55, 56]. Beyond association, prior functional studies provide precedent that macrophage-derived inflammatory cues can directly trigger NETosis, including IL-1β–dependent macrophage–neutrophil crosstalk that promotes NET formation [57, 58]. These reports lend external mechanistic plausibility to our proposed macrophage toNETosis directionality.

These interactions converge on a NETs-enriched, spatially clustered, high-risk microenvironment. NET-derived DNA is sensed by CCDC25 on tumor cells, activating ILK–β-parvin signaling to promote transendothelial migration [59]. Meanwhile, neutrophil elastase (NE) and MMP9 degrade laminins in the extracellular matrix, reactivating dormant tumor cells and fueling recurrence. These mechanisms align with our observed pro-tumor spatial architecture, in which NETs and SPP1$^+$ M2 macrophages are colocalized at the tumor–stroma interface.

Emerging evidence further implicates SPP1 in NETosis during HCC lung metastasis [60]. Specifically, tumor-derived SPP1 acts on alveolar epithelial CD44 to induce CXCL1 expression, thereby recruiting neutrophils and forming a NETs-dominant pre-metastatic niche; in that model, CXCR2 blockade or NET dismantling with DNase I attenuates metastasis [60]. More broadly, NETs have also been shown to fuel HCC metastasis and tumor-associated inflammation, supporting the clinical relevance of NET targeting in HCC [3]. Outside the tumor context, osteopontin has been reported to possess intrinsic pro-NETotic potential in experimental settings [61], further supporting the plausibility that an SPP1-high macrophage niche can be upstream of NET-permissive conditions.

Spatially, we observed consistent co-clustering of SPP1$^+$ M2 macrophages and NETs$^+$ neutrophils at the tumor–stroma interface, suggesting that four conditions—adhesion, chemotaxis, inflammation, and metabolism—are simultaneously fulfilled within the same microenvironmental niche.(i) The OPN–CD44/integrin and ICAM-1–β2-integrin axes form a mechanical scaffold that promotes neutrophil adhesion, retention, and localization within the niche, effectively anchoring these otherwise highly motile cells [62]. (ii) Paracrine inputs from tumor cells, endothelial cells, and CAFs—together with SPP1$^+$ M2—activate and reinforce FAK–PI3K–Akt and NF-κB/MAPK signaling cascades, establishing a local chemotactic and inflammatory amplification loop. (iii) Metabolic inference by decoupleR and scFEA reveals a glycolysis–lactate–glutathione program in SPP1$^+$ M2 that closely mirrors the profile of NETs$^+$ neutrophils, thereby extending the duration of pro-inflammatory signaling and reducing the redox threshold required to trigger NETosis [63].

From a metabolic standpoint, SPP1$^+$ M2 macrophages exhibit heightened glycolysis and lactate accumulation, alongside increased activity in glutathione and purine metabolic pathways. Interestingly, neutrophils exhibiting active NETs phenotypes show similar metabolic flux patterns. This shared "lactate–antioxidant" metabolic landscape not only sustains inflammatory signaling through local acidification and redox buffering but also works synergistically with HIF-1 signaling, endothelial activation, and shear stress to destabilize the microvascular beds. Together, these factors reduce the PAD4-dependent threshold for chromatin decondensation, extending the process of NETosis even in the absence of strong upstream stimuli. In essence, this integrated ecosystem provides a stable, pro-inflammatory environment that may promote metastasis and contribute to therapeutic resistance.

The progressive spatial aggregation and functional coupling of these processes offer an explanation for why deep pathology features consistently identify high-risk biology. These features capture key morphologic hallmarks—such as texture coarsening, boundary disruption, and stromal remodeling—that define the NETs-permissive microdomain.

In exploring the TCM-derived prescription–target network, we find that its mechanisms align closely with our three principal axes, extending beyond a simple drug–gene matching approach. First, at the pathway level, enrichment in extracellular matrix–receptor interactions, the FAK/PI3K–Akt cascade, MAPK, and TNF/IL-17 signaling mirrors the adhesion, chemotaxis, and inflammatory circuits activated by SPP1-positive M2 macrophages. For instance, the matrix and FAK–PI3K–Akt pathways mirror the effects of OPN binding to CD44 and integrins, as well as ICAM-1 signaling via β2 integrins. These inflammatory signals generate the ROS-rich and cytokine-driven environment necessary for NET formation.

Next, network topology highlights important pharmacologic hubs, particularly SRC, AKT1, and CEBPB. SRC and AKT1 are well-established effectors downstream of integrin-mediated adhesion, playing a critical role in cytoskeletal remodeling and inflammatory survival signaling. Meanwhile, CEBPB functions as a transcriptional integrator of inflammation and myeloid differentiation, complementing the NF-κB and MAPK modules that regulate neutrophil priming and NETosis.

Finally, from an ecological perspective, the physicochemical properties of certain herbs—especially those linked to oxidative stress response, wound healing, and anti-inflammation—reflect the redox-rich microenvironment shaped by $SPP1^+$ M2 macrophages. In this environment, where lactate accumulates and antioxidant pressure rises, the threshold for NETosis is lowered, making clearance more challenging. Thus, compounds targeting ROS, adhesion, and inflammatory signaling could effectively disrupt this organizer–effector spatial loop.

In sum, pharmacologic nodes—such as SRC–FAK–AKT, NF-κB/MAPK, and antioxidant pathways—map directly onto the adhesion, inflammation, and metabolic axes that sustain the $SPP1^+$ M2–orchestrated NETs microenvironment.

These findings also highlight clinically tractable intervention points along the $SPP1^+$ M2–NETs axis. NET dismantling via recombinant DNase I (dornase alfa) is already clinically used in other indications and is conceptually aligned with preclinical anti-metastatic NET strategies in HCC [60]. Upstream of NET release, CXCR2/CXCR1–2 blockade is clinically advanced in oncology (e.g., navarixin and reparixin trials) [64, 65], providing a feasible path to reduce neutrophil recruitment/activation in NET-high tumors. IL-8 (CXCL8) neutralization has also been tested clinically in solid tumors [66], supporting the druggability of the CXCL8–CXCR1/2 module emphasized in our communication network. Finally, although cancer-specific evidence is still emerging, osteopontin/SPP1 neutralization has been demonstrated as clinically feasible in humans (safety/PK/PD) in a randomized study [67], suggesting that SPP1-directed strategies could be explored as part of a combinatorial approach in NET-high HCC contexts.

This study retrospectively integrates heterogeneous public datasets. Variability in sample composition, tissue processing, staining, and image acquisition may lead to cross-modal inconsistencies—potentially undermining threshold generalizability and model calibration; additionally, both NETs gene-set activation and adverse histologic features may share upstream drivers such as hypoxia, necrosis, vascular remodeling, infection/inflammation status, or treatment exposure. Methodologically, our NETs classification is transcriptome-derived, denoting a transcriptionally primed but not necessarily fully executed NETosis state; spatial transcriptomics is limited by spot resolution and deconvolution uncertainty (particularly for short-lived neutrophils); ligand–receptor inference based on co-expression does not prove secretion, diffusion, receptor occupancy, or biological activity; and scFEA provides steady-state flux estimates without direct metabolite/ROS quantification or temporal dynamics. Although pseudotime and spatial concordance support a directional hypothesis ($SPP1^+$ M2 → NET-permissive niche), trajectory inference cannot establish causality. Therefore, future studies should include functional validation—e.g., (i) macrophage–neutrophil co-culture or ex vivo slice assays testing whether $SPP1^+$ M2 (or OPN, IL-1β/CXCL8) directly induces NETosis (CitH3/MPO–DNA), (ii) perturbation of SPP1/OPN, CXCR2, IL-1 R/TNFR, or PAD4 pathways, (iii) multiplex spatial imaging/IMC to validate physical interaction and activation states at the tumor–stroma interface, and (iv) targeted metabolomics and redox measurements to confirm the lactate–antioxidant program and its impact on NETosis thresholds.

Conclusions

In this study, we integrated digital pathology with single-cell and spatial transcriptomics to define a NETosis-associated, high-risk ecosystem in hepatocellular carcinoma. Across independent modalities, an $SPP1^+$ M2 macrophage program consistently co-enriched with NETs-related neutrophil signatures at the tumor–stroma interface and aligned with adhesion-, inflammation-, and metabolism-linked signaling circuits. Pseudotime and spatial concordance supported a directional model in which $SPP1^+$ M2 polarization precedes and promotes a

NET-permissive niche, although our evidence remains primarily inferential and requires functional validation. Clinically, these findings highlight tractable intervention points—NET dismantling (DNase I) and inhibition of neutrophil recruitment/activation (e.g., CXCR1/2–CXCL8 axis)—and provide a multi-omic rationale for targeting the SPP1^{+} M2–NETs axis to disrupt high-risk microenvironmental states in HCC.

Acknowledgements
The authors sincerely acknowledge the use of publicly available datasets from the GEO database, which made this research possible.

Authors' contributions
R.L., Y.G., S.H., and S.Z. contributed to the conceptualization, methodology, formal analysis, and original draft preparation. X.Z., W.L., and Z.W. were responsible for software and data curation, while Y.G., R.L., and X.Z. contributed to visualization. W.C., C.C., L.C., and H.D. performed the investigation and validation. M.Z. supervised the study, administered the project, acquired funding, and contributed to review and editing. All authors read and approved the final manuscript.

Funding
This Study was supported by the Open Project Program of NuclearMedicine and Theranostics KeyLaboratory of Sichuan Province(HYX25002).

Data availability
The datasets generated and/or analyzed during the current study are available in the Gene Expression Omnibus (GSE282701: https://www.ncbi.nlm.nih.gov/geo/query/acc.cgi?acc=GSE282701; GSE166635: https://www.ncbi.nlm.nih.gov/geo/query/acc.cgi?acc=GSE166635), the FinnGen Consortium (release R12, finngen_R12_C3_HEPATOCELLU_CARC_EXALLC: https://www.finngen.fi/en/access_results), and the Genome Sequence Archive (HRA000437: https://ngdc.cncb.ac.cn/gsa-human/browse/HRA000437).

Declarations

Ethics approval and consent to participate
Not applicable

Consent for publication
Not applicable

Competing interests
The authors declare that they have no competing interests

Author details
[1]Clinical Medical College, Southwest Medical University, Luzhou 646000, China
[2]School of Nursing, Chongqing College of Humanities, Science & Technology, Chongqing 401524, China
[3]Department of Breast Surgery, The Affliated Hospital, Southwest Medical University, Luzhou 646000, China

Received: 15 October 2025 / Accepted: 12 February 2026
Published online: 24 February 2026

References

1. Chan SL, Sun HC, Xu Y, Zeng H, El-Serag HB, Lee JM, et al. The Lancet commission on addressing the global hepatocellular carcinoma burden: comprehensive strategies from prevention to treatment. Lancet Lond Engl. 2025 Aug 16;406(10504):731–78
2. Global cancer statistics 2022: GLOBOCAN estimates of incidence and mortality worldwide for 36 cancers in 185 countries - bray - 2024 - CA. A cancer journal for clinicians - wiley online library [Internet]. [cited 2026 Jan 15]. Available from: https://acsjournals.onlinelibrary.wiley.com/doi/10.3322/caac.21834.
3. Yang LY, Luo Q, Lu L, Zhu WW, Sun HT, Wei R, et al. Increased neutrophil extracellular traps promote metastasis potential of hepatocellular carcinoma via provoking tumorous inflammatory response. J Hematol Oncol J Hematol Oncol [Internet]. [cited 2025 Oct 5]. 2020 Jan 6;13:3. Available from: https://pmc.ncbi.nlm.nih.gov/articles/PMC6945602/.
4. Jung HS, Gu J, Kim JE, Nam Y, Song JW, Kim HK. Cancer cell-induced neutrophil extracellular traps promote both hypercoagulability and cancer progression. PLoS One [Internet]. [cited 2026 Jan 15]. 2019 Apr 29;14(4):e0216055. Available from: https://pmc.ncbi.nlm.nih.gov/articles/PMC6488070/.
5. Zheng Z, Guan R, Jianxi W, Zhao Z, Peng T, Liu C, et al. Microvascular invasion in hepatocellular carcinoma: a review of its definition, clinical significance, and comprehensive management. J Oncol [Internet]. 2022 Mar 30 [cited 2025 Oct 2], 2022, 9567041. Available from: https://pmc.ncbi.nlm.nih.gov/articles/PMC8986383/
6. Fuchs TA, Brill A, Duerschmied D, Schatzberg D, Monestier M, Myers DD, et al. Extracellular DNA traps promote thrombosis. Proc Natl Acad Sci USA [Internet]. [cited 2025 Oct 5]. 2010 Sept 7;107(36):15880–85. Available from: https://pmc.ncbi.nlm.nih.gov/articles/PMC2936604/.
7. Kaltenmeier C, Yazdani HO, Morder K, Geller DA, Simmons RL, Tohme S. Neutrophil extracellular traps promote T cell exhaustion in the tumor microenvironment. Front immunol [Internet]. 2021 Nov 24 [cited 2025 Oct 5], 12, 785222. Available from: https://pmc.ncbi.nlm.nih.gov/articles/PMC8652262/
8. Saillard C, Schmauch B, Laifa O, Moarii M, Toldo S, Zaslavskiy M, et al. Predicting survival after hepatocellular carcinoma resection using deep learning on histological slides. Hepatology [Internet]. [cited 2026 Jan 15]. 2020 Dec;72(6):2000. Available from: https://journals.lww.com/hep/abstract/2020/12000/predicting_survival_after_hepatocellular_carcinoma.14.aspx.
9. van der Laak J, Litjens G, Ciompi F. Deep learning in histopathology: the path to the clinic. Nat Med [Internet]. [cited 2026 Jan 15]. 2021 May;27(5):775–84. Available from: https://www.nature.com/articles/s41591-021-01343-4.
10. Kather JN, Heij LR, Grabsch HI, Loeffler C, Echle A, Muti HS, et al. Pan-cancer image-based detection of clinically actionable genetic alterations. Nat Cancer [Internet]. [cited 2026 Jan 15]. 2020 Aug;1(8):789–99. Available from: https://pmc.ncbi.nlm.nih.gov/articles/PMC7610412/.
11. Wei J, Chen Z, Hu M, He Z, Jiang D, Long J, et al. Characterizing intercellular communication of Pan-cancer reveals SPP1+ tumor-associated macrophage expanded in hypoxia and promoting cancer malignancy through single-cell RNA-Seq data. Front Cell Dev Biol [Internet]. [cited 2026 Jan 15]. 2021 Oct 5;9:749210. Available from: https://pmc.ncbi.nlm.nih.gov/articles/PMC8523849/.
12. Liu L, Zhang R, Deng J, Dai X, Zhu X, Fu Q, et al. Construction of TME and Identification of crosstalk between malignant cells and macrophages by SPP1 in hepatocellular carcinoma. Cancer Immunol Immunother CII [Internet]. [cited 2026 Jan 15]. 2021 May 24;71(1):121–36. Available from: https://pmc.ncbi.nlm.nih.gov/articles/PMC10992184/.
13. Single-cell and spatial analyses revealed the co-location of cancer stem cells and SPP1+ macrophage in hypoxic region that determines the poor prognosis in hepatocellular carcinoma -. PMC [Internet]. [cited 2025 Oct 2]. Available from: https://pmc.ncbi.nlm.nih.gov/articles/PMC10960828/.
14. Fan G, Xie T, Li L, Tang L, Han X, Shi Y. Single-cell and spatial analyses revealed the co-location of cancer stem cells and SPP1+ macrophage in hypoxic region that determines the poor prognosis in hepatocellular carcinoma. NPJ Precis Oncol [Internet]. [cited 2026 Jan 15]. 2024 Mar 23;8:75. Available from: https://pmc.ncbi.nlm.nih.gov/articles/PMC10960828/.
15. Pang X, He X, Qiu Z, Zhang H, Xie R, Liu Z, et al. Targeting integrin pathways: mechanisms and advances in therapy. Signal Transduct Target Ther [Internet]. [cited 2026 Jan 15]. 2023 Jan 2;8:1. Available from: https://pmc.ncbi.nlm.nih.gov/articles/PMC9805914/.
16. Recombinant human DNase I for the treatment of cancer-associated thrombosis: a pre-clinical study - thrombosis Research [Internet]. [cited 2026 Jan 15]. Available from: https://www.thrombosisresearch.com/article/S0049-3848(21)00321-2/abstract.
17. Gutman DA, Cobb J, Somanna D, Park Y, Wang F, Kurc T, et al. Cancer digital slide Archive: an informatics resource to support integrated in silico analysis of TCGA pathology data. J Am Med Inf Assoc JAMIA [Internet]. [cited 2025 Oct 2]. 2013 Nov;20(6):1091–98. Available from: https://pmc.ncbi.nlm.nih.gov/articles/PMC3822112/.
18. McDonald PC, Topham JT, Awrey S, Tavakoli H, Carroll R, Brown WS, et al. Neutrophil extracellular trap gene expression signatures identify prognostic and targetable signaling axes for inhibiting pancreatic tumour metastasis.

Commun Biol [Internet]. [cited 2025 Oct 15]. 2025 July 4;8:1006. Available from: https://pmc.ncbi.nlm.nih.gov/articles/PMC12227782/.
19. Chen T, Chen X, Zhang S, Zhu J, Tang B, Wang A, et al. The Genome sequence Archive family: toward explosive data growth and diverse data types. Genomics Proteomics Bioinf [Internet]. [cited 2025 Oct 2]. 2021 Aug;19(4):578–83. Available from: https://pmc.ncbi.nlm.nih.gov/articles/PMC9039563/.
20. Kurki MI, Karjalainen J, Palta P, Sipilä TP, Kristiansson K, Donner KM, et al. FinnGen provides genetic insights from a well-phenotyped isolated population. Nature [Internet]. [cited 2025 Oct 2]. 2023;613(7944):508–18. Available from: https://pmc.ncbi.nlm.nih.gov/articles/PMC9849126/.
21. Campanella G, Hanna MG, Geneslaw L, Miraflor A, Werneck Krauss Silva V, Busam KJ, et al. Clinical-grade computational pathology using weakly supervised deep learning on whole slide images. Nat Med. 2019, Aug;25(8):1301–09
22. Ruifrok AC, Johnston DA. Quantification of histochemical staining by color deconvolution. Anal Quant Cytol Histol. 2001, Aug;23(4):291–99
23. Paszke A, Gross S, Massa F, Lerer A, Bradbury J, Chanan G, et al. PyTorch: an imperative style, high-performance deep learning library. Proceedings of the 33rd International Conference on Neural Information Processing Systems. Red Hook, NY, USA: Curran Associates Inc; 2019. 8026–37
24. Ward AO, Janbandhu V, Chapman G, Dunwoodie SL, Harvey RP. An image analysis protocol using CellProfiler for automated quantification of post-ischemic cardiac parameters. Star Protoc [Internet]. [cited 2025 Oct 2]. 2022 Jan 17;3(1):101097. Available from: https://pmc.ncbi.nlm.nih.gov/articles/PMC9076969/.
25. Anghel A, Stanisavljevic M, Andani S, Papandreou N, Rüschoff JH, Wild P, et al. A high-performance System for Robust stain normalization of whole-slide images in histopathology. Front Med [Internet]. [cited 2025 Oct 2]. 2019 Sept 30;6:193. Available from: https://pmc.ncbi.nlm.nih.gov/articles/PMC6778842/.
26. Liu H, Zhang W, Zhang Y, Adegboro AA, Fasoranti DO, Dai L, et al. Mime: a flexible machine-learning framework to construct and visualize models for clinical characteristics prediction and feature selection. Comput Struct Biotechnol J [Internet]. [cited 2025 Oct 2]. 2024 June 29;23:2798–810. Available from: https://pmc.ncbi.nlm.nih.gov/articles/PMC11269309/.
27. Hao Y, Hao S, Andersen-Nissen E, Mauck WM, Zheng S, Butler A, et al. Integrated analysis of multimodal single-cell data. Cell [Internet]. [cited 2025 July 18]. 2021 June 24;184(13):3573–87.e29. Available from: https://www.cell.com/cell/abstract/S0092-8674(21)00583-3.
28. Luecken MD, Theis FJ. Current best practices in single-cell RNA-seq analysis: a tutorial. Mol Syst Biol [Internet]. [cited 2025 Oct 5]. 2019 June 19;15(6):e8746. Available from: https://pmc.ncbi.nlm.nih.gov/articles/PMC6582955/.
29. Zhu Z, Zhang F, Hu H, Bakshi A, Robinson MR, Powell JE, et al. Integration of summary data from GWAS and eQTL studies predicts complex trait gene targets. Nat Genet. 2016, May;48(5):481–87
30. Qiu X, Hill A, Packer J, Lin D, Ma YA, Trapnell C. Single-cell mRNA quantification and differential analysis with census. Nat Methods [Internet]. [cited 2025 Oct 5]. 2017 Mar;14(3):309–15. Available from: https://pmc.ncbi.nlm.nih.gov/articles/PMC5330805/.
31. Ramilowski JA, Goldberg T, Harshbarger J, Kloppman E, Lizio M, Satagopam VP, et al. A draft network of ligand-receptor-mediated multicellular signalling in human. Nat Commun [Internet]. [cited 2025 Oct 2]. 2015 July 22;6:7866. Available from: https://pmc.ncbi.nlm.nih.gov/articles/PMC4525178/.
32. Badia-I-Mompel P, Vélez Santiago J, Braunger J, Geiss C, Dimitrov D, Müller-Dott S, et al. decoupleR: ensemble of computational methods to infer biological activities from omics data. Bioinforma Adv [Internet]. [cited 2025 Oct 2]. 2022 Mar 8;2(1):vbac016. Available from: https://pmc.ncbi.nlm.nih.gov/articles/PMC9710656/.
33. Ma Y, Deng C, Zhou Y, Zhang Y, Qiu F, Jiang D, et al. Polygenic regression uncovers trait-relevant cellular contexts through pathway activation transformation of single-cell RNA sequencing data. Cell Genomics [Internet]. [cited 2025 Oct 2]. 2023 Aug 18;3(9):100383. Available from: https://pmc.ncbi.nlm.nih.gov/articles/PMC10504677/.
34. Cable DM, Murray E, Zou LS, Goeva A, Macosko EZ, Chen F, et al. Robust decomposition of cell type mixtures in spatial transcriptomics. Nat Biotechnol [Internet]. [cited 2025 Oct 2]. 2022 Apr;40(4):517–26. Available from: https://pmc.ncbi.nlm.nih.gov/articles/PMC8606190/.
35. Seal RL, Braschi B, Gray K, Jones TEM, Tweedie S, Haim-Vilmovsky L, et al. Genenames.Org: the HGNC resources in 2023. Nucleic Acids Res [Internet]. [cited 2025 Oct 2]. 2023 Jan 6;51:D1D1003–9). Available from: https://doi.org/10.1093/nar/gkac888.
36. Demers M, Wong SL, Martinod K, Gallant M, Cabral JE, Wang Y, et al. Priming of neutrophils toward NETosis promotes tumor growth. Oncoimmunology [Internet]. [cited 2025 Oct 2]. 2016 Feb 18;5(5):e1134073. Available from: https://pmc.ncbi.nlm.nih.gov/articles/PMC4910712/.
37. Leal AC, Mizurini DM, Gomes T, Rochael NC, Saraiva EM, Dias MS, et al. Tumor-derived exosomes induce the formation of neutrophil extracellular traps: implications for the establishment of cancer-associated thrombosis. Sci Rep [Internet]. [cited 2025 Oct 2]. 2017 July 25;7:6438. Available from: https://pmc.ncbi.nlm.nih.gov/articles/PMC5526939/.
38. Su X, Brassard A, Bartolomucci A, Dhoparee-Doomah I, Qiu Q, Tsering T, et al. Tumour extracellular vesicles induce neutrophil extracellular traps to promote lymph node metastasis. J Extracell Vesicles [Internet]. [cited 2025 Oct 5]. 2023 Aug;12(8):12341. Available from: https://pmc.ncbi.nlm.nih.gov/articles/PMC10415595/.
39. Almyroudis NG, Grimm MJ, Davidson BA, Röhm M, Urban CF, Segal BH. Netosis and NADPH oxidase: at the intersection of host defense, inflammation, and injury. Front Immunol [Internet]. [cited 2025 Oct 2]. 2013 Mar 1;4:45. Available from: https://pmc.ncbi.nlm.nih.gov/articles/PMC3585429/.
40. Wang Y, Li M, Stadler S, Correll S, Li P, Wang D, et al. Histone hypercitrullination mediates chromatin decondensation and neutrophil extracellular trap formation. J Cell Biol [Internet]. [cited 2025 Oct 5]. 2009 Jan 26;184(2):205–13. Available from: https://pmc.ncbi.nlm.nih.gov/articles/PMC2654299/.
41. Röhm M, Grimm MJ, D'Auria AC, Almyroudis NG, Segal BH, Urban CF. NADPH oxidase promotes neutrophil extracellular trap formation in pulmonary aspergillosis. Infect Immun [Internet]. [cited 2025 Oct 2]. 2014 May;82(5):1766–77. Available from: https://pmc.ncbi.nlm.nih.gov/articles/PMC3993456/.
42. Papayannopoulos V, Metzler KD, Hakkim A, Zychlinsky A. Neutrophil elastase and myeloperoxidase regulate the formation of neutrophil extracellular traps. J Cell Biol [Internet]. [cited 2025 Oct 5]. 2010 Nov 1;191(3):677. Available from: https://pmc.ncbi.nlm.nih.gov/articles/PMC3003309/.
43. Ozel I, Sha G, Będzińska A, Pylaeva E, Naumova Y, Thiel I, et al. Neutrophil-specific targeting of STAT3 impairs tumor progression via the expansion of cytotoxic CD8+ T cells. Signal Transduct Target Ther [Internet]. [cited 2025 Oct 5]. 2025 Aug 30;10:279. Available from: https://pmc.ncbi.nlm.nih.gov/articles/PMC12398498/.
44. Bell E. Neutrophil NETworks. Nat Rev Immunol [Internet]. [cited 2025 Oct 5]. 2004 Apr;4(4):244–244. Available from: https://www.nature.com/articles/nri1340.
45. Ma Y, Wei J, He W, Ren J. Neutrophil extracellular traps in cancer. MedComm [Internet]. [cited 2025 Oct 2]. 2024 July 15;5(8):e647. Available from: https://pmc.ncbi.nlm.nih.gov/articles/PMC11247337/.
46. Martinod K, Wagner DD. Thrombosis: tangled up in NETs. Blood [Internet]. [cited 2026 Jan 16]. 2014 May 1;123(18):2768–76. Available from: https://pmc.ncbi.nlm.nih.gov/articles/PMC4007606/.
47. Jiménez-Alcázar M, Rangaswamy C, Panda R, Bitterling J, Simsek YJ, Long AT, et al. Host DNases prevent vascular occlusion by neutrophil extracellular traps. Science [Internet]. [cited 2026 Jan 16]. 2017 Dec;358(6367):1202–06. Available from: https://www.science.org/doi/10.1126/science.aam8897.
48. Yan Z, Hu X, Tang B, Deng F. Role of osteopontin in cancer development and treatment. Heliyon [Internet]. [cited 2025 Oct 2]. 2023 Oct 14;9(10):e21055. Available from: https://pmc.ncbi.nlm.nih.gov/articles/PMC10587537/.
49. Yokosaki Y, Matsuura N, Sasaki T, Murakami I, Schneider H, Higashiyama S, et al. The integrin alpha(9)beta(1) binds to a novel recognition sequence (SVVYGLR) in the thrombin-cleaved amino-terminal fragment of osteopontin. J Biol Chem. 1999, Dec, 17;274(51):36328–34
50. Lamort AS, Giopanou I, Psallidas I, Stathopoulos GT. Osteopontin as a link between inflammation and cancer: the thorax in the spotlight. Cells [Internet]. [cited 2025 Oct 2]. 2019 Aug 2;8(8):815. Available from: https://pmc.ncbi.nlm.nih.gov/articles/PMC6721491/.
51. Neutrophil extracellular traps promote differentiation and function of fibroblasts - chrysanthopoulou - 2014 -. The J Pathol - Wiley Online Lib [Internet]. [cited 2026 Jan 16]. Available from: https://pathsocjournals.onlinelibrary.wiley.com/doi/10.1002/path.4359.
52. Keikhosravi A, Li B, Liu Y, Conklin MW, Loeffler AG, Eliceiri KW. Non-disruptive collagen characterization in clinical histopathology using cross-modality image synthesis. Commun Biol [Internet]. [cited 2026 Jan 16]. 2020 July 31;3:414. Available from: https://pmc.ncbi.nlm.nih.gov/articles/PMC7395097/.
53. Ahmed M, Kundu GC. Osteopontin selectively regulates p70S6K/mTOR phosphorylation leading to NF-κB dependent AP-1-mediated ICAM-1 expression in breast cancer cells. Mol Cancer [Internet]. [cited 2025 Oct 2]. 2010 May 7;9:101. Available from: https://pmc.ncbi.nlm.nih.gov/articles/PMC2881115/.

54. Bui TM, Wiesolek HL, Sumagin R. ICAM-1: a master regulator of cellular responses in inflammation, injury resolution, and tumorigenesis. J Leukoc Biol [Internet]. [cited 2025 Oct 2]. 2020 Sept;108(3):787–99. Available from: https://pmc.ncbi.nlm.nih.gov/articles/PMC7977775/.
55. Rahman A, Fazal F. Hug tightly and say goodbye: role of endothelial ICAM-1 in leukocyte transmigration. Antioxid Redox Signal [Internet]. [cited 2025 Oct 2]. 2009 Apr;11(4):823–39. Available from: https://pmc.ncbi.nlm.nih.gov/articles/PMC2850296/.
56. An Z, Li J, Yu J, Wang X, Gao H, Zhang W, et al. Neutrophil extracellular traps induced by IL-8 aggravate atherosclerosis via activation NF-κB signaling in macrophages. Cell Cycle [Internet]. [cited 2025 Oct 2]. 2019 Sept 8;18(21):2928–38. Available from: https://pmc.ncbi.nlm.nih.gov/articles/PMC6791689/.
57. Yalcinkaya M, Fotakis P, Liu W, Endo-Umeda K, Dou H, Abramowicz S, et al. Cholesterol accumulation in macrophages drives NETosis in atherosclerotic plaques via IL-1β secretion. Cardiovasc Res [Internet]. [cited 2026 Jan 16]. 2022 Dec 20;119(4):969–81. Available from: https://pmc.ncbi.nlm.nih.gov/articles/PMC10153645/.
58. Sil P, Wicklum H, Surell C, Rada B. Macrophage-derived IL-1β enhances monosodium urate crystal-triggered NET formation. Inflamm Res Off J Eur Histamine Res Soc Al [Internet]. [cited 2026 Jan 16]. 2017 Mar;66(3):227–37. Available from: https://pmc.ncbi.nlm.nih.gov/articles/PMC5296223/.
59. Albrengues J, Shields M, Ng D, Park CG, Ambrico A, Poindexter M, et al. Neutrophil extracellular traps produced during inflammation awaken dormant cancer cells in mice. Science [Internet]. [cited 2025 Oct 2]. 2018 Sept 28;361(6409):eaao4227. Available from: https://pmc.ncbi.nlm.nih.gov/articles/PMC6777850/.
60. Xie SZ, Yang LY, Wei R, Shen XT, Pan JJ, Yu SZ, et al. Targeting SPP1-orchestrated neutrophil extracellular traps-dominant pre-metastatic niche reduced HCC lung metastasis. Exp Hematol Oncol [Internet]. [cited 2025 Oct 5]. 2024 Nov 11;13:111. Available from: https://pmc.ncbi.nlm.nih.gov/articles/PMC11556024/.
61. Bertolotto M, Verzola D, Contini P, de TD, Tirandi A, Ramoni D, et al. Osteopontin is associated with neutrophil extracellular trap formation in elderly patients with severe sepsis. [cited 2026 Jan 16]; Available from: https://onlinelibrary.wiley.com/doi/10.1111/eci.14159.
62. Choi EY, Santoso S, Chavakis T. Mechanisms of neutrophil transendothelial migration. Front Biosci J Virtual Libr [Internet]. [cited 2025 Oct 2]. 2009 Jan 1;14:1596–605. Available from: https://pmc.ncbi.nlm.nih.gov/articles/PMC2672407/.
63. Awasthi D, Nagarkoti S, Sadaf S, Chandra T, Kumar S, Dikshit M. Glycolysis dependent lactate formation in neutrophils: a metabolic link between NOX-dependent and independent NETosis. Biochim Biophys Acta Mol Basis Dis. 2019, Dec, 1;1865(12):165542
64. Armstrong AJ, Geva R, Chung HC, Lemech C, Miller WH Jr, Hansen AR, et al. CXCR2 antagonist navarixin in combination with pembrolizumab in select advanced solid tumors: a phase 2 randomized trial. Invest New Drugs [Internet]. [cited 2026 Jan 16]. 2024;42(1):145–59. Available from: https://pmc.ncbi.nlm.nih.gov/articles/PMC11076327/.
65. Goldstein LJ, Perez RP, Yardley D, Han LK, Reuben JM, Gao H, et al. A window-of-opportunity trial of the CXCR1/2 inhibitor reparixin in operable HER-2-negative breast cancer. Breast Cancer Res BCR [Internet]. [cited 2026 Jan 16]. 2020;22:4. Available from: https://pmc.ncbi.nlm.nih.gov/articles/PMC6954543/.
66. Bilusic M, Heery CR, Collins JM, Donahue RN, Palena C, Madan RA, et al. Phase I trial of HuMax-IL8 (BMS-986253), an anti-IL-8 monoclonal antibody, in patients with metastatic or unresectable solid tumors. J Immunother Cancer [Internet]. [cited 2026 Jan 16]. 2019 Sept 5;7:240. Available from: https://pmc.ncbi.nlm.nih.gov/articles/PMC6729083/.
67. Boumans MJH, Houbiers JGA, Verschueren P, Ishikura H, Westhovens R, Brouwer E, et al. Safety, tolerability, pharmacokinetics, pharmacodynamics and efficacy of the monoclonal antibody ASK8007 blocking osteopontin in patients with rheumatoid arthritis: a randomised, placebo controlled, proof-of-concept study. Ann Rheum Dis [Internet]. [cited 2026 Jan 16]. 2012 Feb 1;71(2):180–85. Available from: https://ard.eular.org/article/S0003-4967(24)18981-9/abstract.

Publisher's Note